

CROM: Continuous Reduced-Order Modeling of PDEs Using Implicit Neural Representations

Peter Yichen Chen¹Jinxu Xiang¹Dong Heon Cho¹G A Pershing¹Henrique Teles Maia¹Maurizio Chiaramonte²Kevin Carlberg²Eitan Grinspun^{3,1}¹Columbia University²Meta Reality Labs Research³University of Toronto

Abstract

The excessive runtime of high-fidelity partial differential equation (PDE) solvers makes them unsuitable for time-critical applications. We propose to accelerate PDE solvers using reduced-order modeling (ROM). Whereas prior ROM approaches reduce the dimensionality of *discretized* vector fields, our *continuous* reduced-order modeling (CROM) approach builds a smooth, low-dimensional manifold of the *continuous* vector fields themselves, not their discretization. We represent this reduced manifold using neural fields, relying on their continuous and differentiable nature to efficiently solve the PDEs. CROM may train on any and all available numerical solutions of the continuous system, even when they are obtained using diverse methods or discretizations. After the low-dimensional manifolds are built, solving PDEs requires significantly less computational resources. Since CROM is discretization-agnostic, CROM-based PDE solvers may optimally adapt discretization resolution over time to economize computation. We validate our approach on an extensive range of PDEs with training data from voxel grids, meshes, and point clouds. Large-scale experiments demonstrate that our approach obtains speed, memory, and accuracy advantages over prior ROM approaches while gaining $109\times$ wall-clock speedup over full-order models on CPUs and $89\times$ speedup on GPUs.

1 Introduction

Many scientific and engineering models are posed as partial differential equations (PDEs) of the form

$$\mathcal{F}(\mathbf{f}, \nabla \mathbf{f}, \nabla^2 \mathbf{f}, \dots, \dot{\mathbf{f}}, \ddot{\mathbf{f}}, \dots) = 0, \quad \mathbf{f}(\mathbf{x}, t) : \Omega \times \mathcal{T} \rightarrow \mathbb{R}^d, \quad (1)$$

where \mathbf{f} is a spatiotemporal dependent, multidimensional continuous vector field, such as temperature, velocity, or displacement; ∇ and (\cdot) are the spatial and temporal gradients; $\Omega \subset \mathbb{R}^m$ and $\mathcal{T} \subset \mathbb{R}$ are the spatial and temporal domains, respectively.

We may solve for \mathbf{f} by discretizing in space, $\mathbf{f}(\mathbf{x}, t) \approx \mathbf{f}_P(\mathbf{x}, t) = \sum_{i=1}^P \mathbf{a}^i(t) N^i(\mathbf{x})$, transforming the continuous spatial representation to a $(P \cdot d)$ -dimensional vector whose coefficients $\mathbf{a}^i(t) : \mathcal{T} \rightarrow \mathbb{R}^d$ and the corresponding basis functions $N^i(\mathbf{x}) : \Omega \rightarrow \mathbb{R}$ (e.g., polynomial basis, fourier basis) approximate the continuous solution. For instance, if N^i is the linear finite element basis, the coefficients $\mathbf{a}^i(t) = \mathbf{f}(\mathbf{x}^i, t)$ are field values at spatial samples \mathbf{x}^i (Hughes, 2012).

After introducing temporal samples $\{t_n\}_{n=0}^T$, we temporally evolve the solution by solving for P unknowns $\{\mathbf{a}^i(t_{n+1})\}$ given the previous state $\{\mathbf{a}^i(t_n)\}$. Unfortunately, when P is large, processing and memory costs of these *full-order* solves become intractable. To alleviate this computational burden, prior model reduction techniques (Berkooz et al., 1993; Willcox and Peraire, 2002; Benner et al., 2015) construct a manifold $\mathbf{g}_P : \mathbb{R}^r \rightarrow \mathbb{R}^{Pd}$, with $r \ll Pd$, such that every latent space vector

Preprint. Under review.

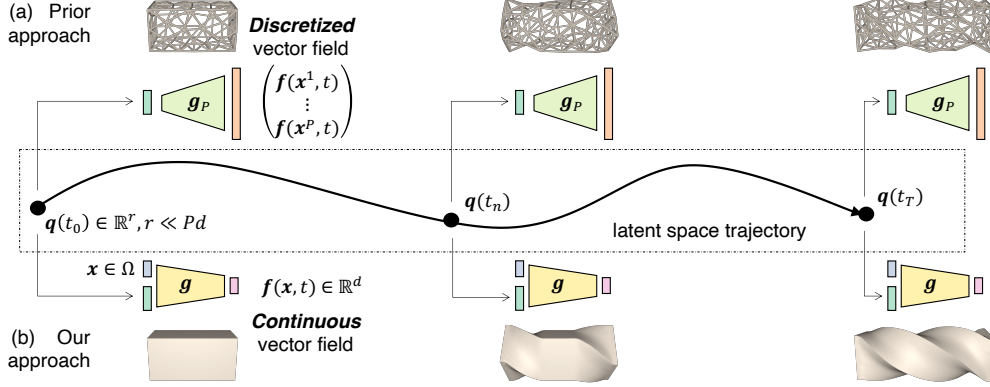


Figure 1: Model reduction solves PDEs via temporal evolution of the low-dimensional latent space vector $q(t)$. (a) Prior work assumes that the low-dimensional representation g_P is built for the *already-discretized* vector field; (b) our approach constructs the low-dimensional manifold g directly for the *continuous* vector field. In this case, the vector field f represents the twisting material governed by the elastodynamics equation.

$q(t) \in \mathbb{R}^r$ maps to a discrete field $g_P(q) \mapsto (a^1, \dots, a^P)^T$. For instance, for linear finite elements (Barbič and James, 2005), $g_P(q) \mapsto (f(x^1, t), \dots, f(x^P, t))^T$, as depicted in Figure 1a. ROM saves computation because we evolve only $r \ll Pd$ latent space variables.¹

Since existing ROM approaches apply to *already-discretized* fields, model training and PDE solving are tied to the dimension and discretization type of the training data, engendering key limitations:

1. If we alter the training simulation resolution (P) or the discretization types (e.g., from meshes to point clouds), we have to rebuild the manifold with different architectures and numbers of parameters.
2. If we increase the number of discretized samples (P), the memory usage surges as the output dimension increases.
3. After the manifold is built and whenever solving PDEs on this manifold, we cannot adaptively update the spatial resolution (P), discretization types, or the basis function (N^i).
4. We do not have information about the spatial gradients of the vector field (∇f) or the degrees of freedom outside the ones used for constructing the manifold.

These problems arise because $g_P(q) \mapsto (a^1, \dots, a^P)^T$ produces a discretized output. We overcome these limitations by formulating the low-dimensional manifold $g(q, x) \approx f(x, t)$ as approximating the *continuous* field itself, *not* its discretization (see Figure 1b). In doing so, our reduction becomes independent of the discretization employed for model training and/or PDE solving.

In this work, we propose to represent $g(q, x)$ as an implicit neural representation (Park et al., 2019; Chen and Zhang, 2019; Mescheder et al., 2019), also known as a neural field, as the resulting field is smooth and analytically-differentiable; however, other representations of continuously differentiable functions could be explored.

We experimentally test the framework on PDEs from thermodynamics, image processing, fluid dynamics, and solid mechanics, with discretized data from voxel grids, meshes, and point clouds. After the manifold is built, we solve the PDEs by computing latent space dynamics. Large-scale examples demonstrate that the reduced-order model offers 41-109 \times speedup over the full-order model across different computing architectures.

2 Related Work

Model reduction of PDEs was recently surveyed by Benner et al. (2015). Well-known low-dimensional manifold construction schemes include rational interpolation (Bai, 2002), balanced

¹Latent space vector is also known as the feature space vector, subspace vector, or generalized coordinates.

truncation (Moore, 1981), and proper orthogonal decomposition (POD) (Lumley, 1967; Sirovich, 1987; Berkooz et al., 1993). Linear methods such as principal component analysis (PCA) have been the mainstay, but recent work has explored neural-network based methods (Fulton et al., 2019; Kim et al., 2019; Wiewel et al., 2019; Lee and Carlberg, 2020; Shen et al., 2021). *All* of these prior works exclusively construct the low-dimensional manifold for the *discretization* of the vector field. To the best of our knowledge, only the concurrent works by Chen et al. (2021), Pan et al. (2022) build a low-dimensional manifold directly for the *continuous* vector field. Chen et al. (2021)’s treatment specializes to the material point method (discretization) and elasticity (PDE); our general treatment is both discretization and PDE agnostic. Pan et al. (2022) *train* a latent space for PDE data; we further *solve* the PDEs in reduced space via rapid latent space traversal.

Implicit neural representations use (fully-connected) neural networks to represent arbitrary vector fields, from signed distance fields (Park et al., 2019; Chen and Zhang, 2019; Mescheder et al., 2019) to radiance fields (Mildenhall et al., 2020). While the Euclidean space spatial coordinates always form part of the input to the network, it is also common to have a latent space vector to form the rest of the input. For example, different latent space vectors may correspond to different geometries and view-dependent radiance fields. We likewise adopt the spatial coordinates and latent space vector split for our input. In the same spirit, our work’s latent space vector also corresponds to different states of the continuous vector field (see Figure 1b).

Machine learning (ML) for PDEs. Sinusoidal representation network (SIREN) by Sitzmann et al. (2020b) and physics-informed neural network (PINN) by Raissi et al. (2019) both demonstrate that PDEs can be accurately solved via neural representations. However, the degrees of freedom involved in their approaches are still Pd , and the underlying gradient-descent-based solver is often computationally more *expensive* than traditional solvers. By contrast, our goal is building a computationally more *efficient* solution that solves for only r degrees of freedom ($r \ll Pd$). In fact, our approach can be viewed as an extension of SIREN and PINN for model reduction. Setting the latent space vector $\mathbf{q}(t)$ in our formulation (see Figure 1b) to the time variable t recovers the exact formulation of SIREN and PINN. Considering another architecture, Sanchez-Gonzalez et al. (2020) show graph neural network (GNN)’s capability of learning PDEs. Like SIREN and PINN, GNN does not offer dimension reduction.

3 Method: Overview and Manifold Construction

Overview Our goal is to efficiently obtain the solution of Equation (1). We begin by constructing a low dimensional manifold (see below), after which we solve PDEs by integrating in time the dynamics of the manifold’s latent space vector (see Section 4). As we demonstrate in examples from four scientific disciplines (see Section 5), this general method is applicable regardless of the discretizations of the training data (e.g., voxel grids, meshes, point clouds) or the discretizations deemed most useful for evaluating the gradients (e.g., physical forces) when solving PDEs on the constructed manifold.

Low-dimensional Manifold Construction As depicted in Figure 1b, we seek a manifold $\mathbf{g}(\mathbf{x}, \mathbf{q})$,

$$\mathbf{g}(\mathbf{x}, \mathbf{q}(t; \boldsymbol{\mu})) \approx \mathbf{f}(\mathbf{x}, t; \boldsymbol{\mu}), \quad \forall \mathbf{x} \in \Omega, \quad \forall t \in \mathcal{T}, \quad \forall \boldsymbol{\mu} \in \mathcal{D}, \quad (2)$$

that well approximates the continuous field $\mathbf{f}(\mathbf{x}, t; \boldsymbol{\mu})$ throughout the spatiotemporal domain $\Omega \times \mathcal{T}$, and for a workable range of problem parameters $\boldsymbol{\mu} \in \mathcal{D}$. For ease of exposition, we omit the dependencies of \mathbf{q} and \mathbf{f} on the problem parameters $\boldsymbol{\mu}$. Here \mathcal{D} is an arbitrary parameter space (e.g., material properties, external forces, user settings). For scenarios that do not feature trivial parameterizations, e.g., external force via crowd-sourcing (Barbič and James, 2005), \mathcal{D} can also be implicitly defined.

What distinguishes our approach from typical model reduction is that \mathbf{g} takes the position $\mathbf{x} \in \Omega$ as an input. Thus, unlike prior approaches that infer only discrete coefficients, our approach infers field values at arbitrary domain positions \mathbf{x} .

To implement the manifold, we parameterize \mathbf{g} with a neural network \mathbf{g}_{θ_g} . The network’s weights θ_g can be trained by optimizing the following minimization problem:

$$\min_{\theta_g} \sum_{i=1, \dots, P, \quad n=0, \dots, T, \quad \boldsymbol{\mu} \in \mathcal{D}_{\text{train}}} \|\mathbf{g}_{\theta_g}(\mathbf{x}^i, \mathbf{q}(t_n)) - \mathbf{f}(\mathbf{x}^i, t_n)\|_2^2, \quad (3)$$

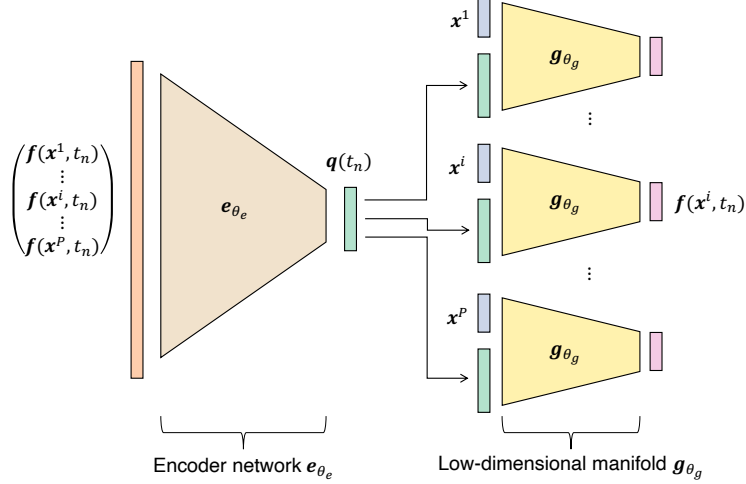


Figure 2: Constructing the low-dimensional manifold as a neural network trained via supervised learning. We pass each snapshot (time step) from the training dataset into an encoder to obtain a latent space vector \mathbf{q} . We then concatenate \mathbf{q} with the spatial coordinates and pass that into the low-dimensional manifold with the goal of reconstructing \mathbf{f} for each individual spatial sample. The same \mathbf{q} is shared among all spatial samples in this time step.

where $\mathcal{D}_{\text{train}} \subset \mathcal{D}$ is the training set; $\mathbf{q}(t_n)$ is the latent space vector shared among all spatial samples. Essentially, we aim to reconstruct all the vector field samples in the training data.

The training data is generated via full-order PDE solvers. Notably, our approach imposes no limit on the discretization strategy of these PDE solvers. For instance, this framework is applicable to training data from both finite difference methods and finite element methods as well as both voxel grids and meshes.

There are commonly two approaches to define the latent space vector \mathbf{q} : the auto-decoder approach (Park et al., 2019) that trains \mathbf{q} along with \mathbf{g}_{θ_g} and the encoder approach (Chen and Zhang, 2019; Mescheder et al., 2019) that trains a separate network to output \mathbf{q} . While both approaches work for our application, we adopt the latter.

The encoder network e_{θ_e} with weights θ_e takes an input vector constructed by concatenating all the discrete degrees of freedom from the training data and outputs a latent space vector (see Figure 2):

$$e_{\theta_e}(\vec{\mathbf{f}}(t)) = \mathbf{q}(t), \quad \text{where } \vec{\mathbf{f}}(t) = (\mathbf{f}(\mathbf{x}^1, t), \dots, \mathbf{f}(\mathbf{x}^i, t), \dots, \mathbf{f}(\mathbf{x}^P, t))^T.$$

We emphasize that this discretization-dependent encoder (Xie et al., 2021) is merely a tool for training the smoothly varying latent space. The implicit neural representation \mathbf{g}_{θ_g} remains discretization-agnostic.

Adding the encoder, Equation (3) now becomes

$$\min_{\theta_g, \theta_e} \sum_{i=1, \dots, P, n=0, \dots, T, \mu \in \mathcal{D}_{\text{train}}} \|\mathbf{g}_{\theta_g}(\mathbf{x}^i, e_{\theta_e}(\vec{\mathbf{f}}(t_n))) - \mathbf{f}(\mathbf{x}^i, t_n)\|_2^2 \quad (4)$$

Figure 2 illustrates the entire training pipeline. Further network and training details are listed in the supplement.

4 Method: Latent Space Dynamics

After the manifold is constructed, we compute latent space dynamics ($\mathbf{q}_n \rightarrow \mathbf{q}_{n+1}$) in three steps (see Figure 3): (1) network inference, (2) PDE time-stepping, and (3) network inversion. Notably, in our approach, the neural network strictly serves as a *spatial* representation for (1) and (3). The network does not model the PDE time integration (2). Therefore, the time evolution itself is driven by the original PDE. We do not approximate established laws of physics with neural networks.

Commonly shared among all three steps are “integration samples,” a finite set of spatial domain points $\mathcal{M} := \{\mathbf{y}^j \in \Omega \mid 1 \leq j \leq |\mathcal{M}|\}$ chosen at the user’s discretion (see Section 4.4). These samples

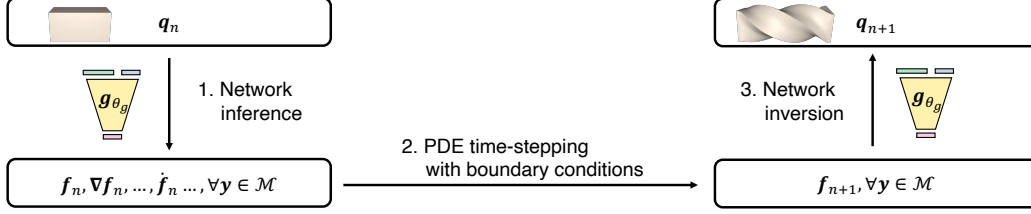


Figure 3: Latent space dynamics: temporally evolve from one latent space vector to another, governed by the PDE. The entire pipeline only involves degrees of freedom from a small spatial subset \mathcal{M} , where $|\mathcal{M}| \ll P$.

need not coincide with the full-order discretization samples $\{\mathbf{x}^i\}_{i=1}^P$ mentioned as an example of linear finite element discretization; this is in stark contrast with existing model reduction literature that only supports hyper-reduction samples attached to the full-order discretization from the training data.

4.1 Network Inference

We first aim to gather all the full-space spatiotemporal information ($\forall \mathbf{y} \in \mathcal{M}$) necessary for PDE time integration. The function value \mathbf{f} itself can be evaluated via inferencing of the neural network $\mathbf{f}(\mathbf{y}, t_n) = g_{\theta_g}(\mathbf{y}, \mathbf{q}_n)$. The spatial and temporal gradients are computed either by differentiating the network, $\nabla \mathbf{f}(\mathbf{y}, t_n) = \nabla_{\mathbf{x}} g_{\theta_g}$ and $\dot{\mathbf{f}}(\mathbf{y}, t_n) = \frac{\partial g_{\theta_g}}{\partial \mathbf{q}} \dot{\mathbf{q}}_n$, respectively, or by numerical approximation. Higher-order gradients may be generalized in a similar manner. Further details on gradient computation are listed in the supplement.

4.2 PDE Time-stepping

Next, our goal is to calculate $\mathbf{f}(\mathbf{y}, t_{n+1}), \forall \mathbf{y} \in \mathcal{M}$.

For each integration sample, we solve for $\dot{\mathbf{f}}_{n+1}, \dots$ from the temporal discretization of Equation (1):

$$\mathcal{F}(\mathbf{f}_n, \nabla \mathbf{f}_n, \dots, \dot{\mathbf{f}}_{n+1}, \dots) = \mathbf{0}. \quad (5)$$

We assume an explicit-time (t_n) treatment of \mathbf{f} and its spatial gradients. In addition, we also enforce proper (e.g., Dirichlet, Neumann) boundary conditions.

Afterwards, we integrate each sample temporally to obtain \mathbf{f}_{n+1} ,

$$\mathbf{f}_{n+1} = \mathcal{I}(\Delta t, \mathbf{f}_n, \dot{\mathbf{f}}_{n+1}, \dots), \quad (6)$$

where $\Delta t = t_{n+1} - t_n$ is the time step size; \mathcal{I} can be any temporal integration scheme, e.g., Runge-Kutta methods (Dormand and Prince, 1980).

4.3 Network Inversion

Lastly, we invert the network, finding the corresponding input \mathbf{q}_{n+1} that matches the newly computed \mathbf{f}_{n+1} , by solving the least-squares problem

$$\min_{\mathbf{q}_{n+1} \in \mathbb{R}^r} \sum_{\mathbf{y} \in \mathcal{M}} \|g_{\theta_g}(\mathbf{y}, \mathbf{q}_{n+1}) - \mathbf{f}(\mathbf{y}, t_{n+1})\|_2^2. \quad (7)$$

The objective is similar to the training loss found in Equation (3), but with two dimensions significantly reduced: the dimension of the unknown \mathbf{q}_{n+1} , and the summation bound $|\mathcal{M}|$. Consequently, instead of using a stochastic gradient descent type of method, such as the auto-decoder scheme by Park et al. (2019), we achieve rapid network inversion using the Gauss-Newton algorithm (Nocedal and Wright, 2006) with conditionally quadratic convergence. Further details are listed in the supplement.

4.4 Spatial Sample Reduction

The least squares formulation from Equation (7) is well-posed if $r \leq d|\mathcal{M}|$. Since the low-dimensional manifold construction guarantees that $r \ll Pd$, we choose $\frac{r}{d} \leq |\mathcal{M}| \ll P$. To

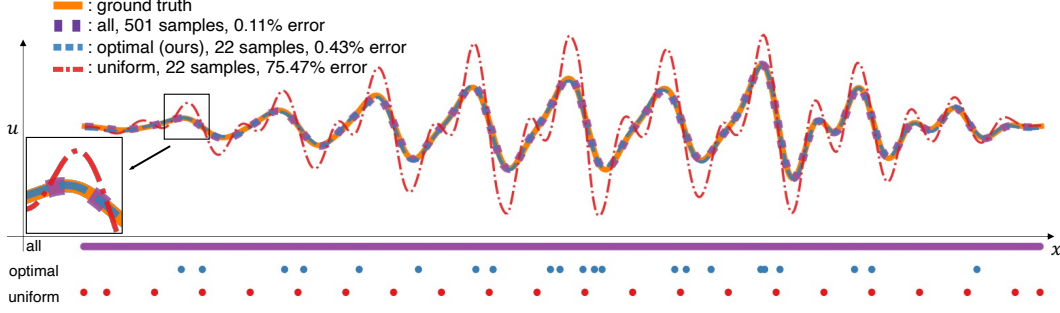


Figure 4: Thermodynamics: integration samples (\mathcal{M}). Optimally selecting the samples (blue) allows us to use significantly fewer degrees of freedom than the full-order simulation (purple) while getting a much higher accuracy than naive uniform sampling (red). The particular vector field shown is the temperature governed by the heat equation after 100 time steps.

obtain the next-time step $\mathbf{f}(\mathbf{y}, t_{n+1}), \forall \mathbf{y} \in \mathcal{M}$ necessary for the least squares solves, we only require PDE updates (Section 4.2) and spatiotemporal data (Section 4.1) at these $|\mathcal{M}|$ samples. As such, the entire latent space dynamics framework (Figure 3) only requires $|\mathcal{M}|$ samples. Thus, we have obtained a spatial sample reduction from the full-order solver's P to $|\mathcal{M}|$.

A naive selection of the integration samples would lead to inaccurate latent space dynamics, even if $|\mathcal{M}| \geq \frac{r}{d}$. Figure 4 demonstrates a failure case where the integration samples are naively chosen uniformly throughout the space. In practice, we find stochastic sampling would eliminate such an error, consistent with the hyper-reduction strategies from existing model reduction literature (Carlberg, 2011). To further guarantee the correctness of the latent space dynamics, we develop an optimal sampling scheme. Given a target latent space dynamics accuracy, our scheme greedily selects integration samples until the target accuracy is satisfied. Figures 4, 6 and 9 display the superior performances of our sampling strategies. Further details are listed in the supplement.

5 Experiments

We analyze the proposed framework on PDEs arising from four disciplines, with training data produced using a variety of discretizations (voxel grids, meshes, and point clouds). For each PDE, we delineate a testing set where $\mathcal{D}_{\text{test}} \subset \mathcal{D}$ with $\mathcal{D}_{\text{train}} \cap \mathcal{D}_{\text{test}} = \emptyset$. We always construct the manifold (Section 3) with data from $\mathcal{D}_{\text{train}}$, and then validate the latent space dynamics (Section 4) on $\mathcal{D}_{\text{test}}$. Unless otherwise noted, all errors reported are relative errors, i.e., $\sqrt{\|\mathbf{f} - \mathbf{f}_{gt}\|^2 / \|\mathbf{f}_{gt}\|^2}$. The supplement contains implementation and reproducibility details for each PDE investigated below. The temporal evolutions of the PDEs are best illustrated via the **supplementary video**.

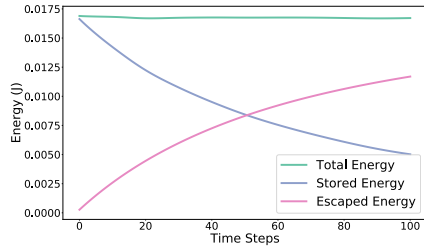


Figure 5: Thermodynamics: the reduced simulation in Figure 4 conserves total heat energy over time (green line).

Thermodynamics $\frac{\partial u}{\partial t} - \nu(x) \frac{\partial^2 u}{\partial x^2} = 0$ Temperature u is the continuous vector field of interest and is governed by a 1D heat equation. ν describes the spatially-varying diffusion speed. Figure 4 displays how our approach accurately represents the diffused temperature while using significantly fewer integration samples than the full-order model. Figure 5 further demonstrates that the reduced simulation faithfully captures the conservation of heat energy over time.

Image Processing $\frac{\partial u}{\partial t} - \nu(x) \nabla^2 u = 0$ We model image blurring with the 2D diffusion equation (Perona and Malik, 1990). Figure 6 exhibits our method's ability to robustly capture blurring in spatially-varying parts of the image.

Fluid Dynamics $\frac{\partial \mathbf{u}}{\partial t} + (\mathbf{u} \cdot \nabla) \mathbf{u} = -\nabla p + \nu \nabla^2 \mathbf{u} + \mathbf{f}_{ext}, \nabla \cdot \mathbf{u} = 0$ We solve the incompressible Navier-Stokes equations for fluid velocity \mathbf{u} , where p is the pressure and \mathbf{f}_{ext} is the external force. Figure 7 displays how our CROM approach properly models the detailed vortices of the fluid flow.

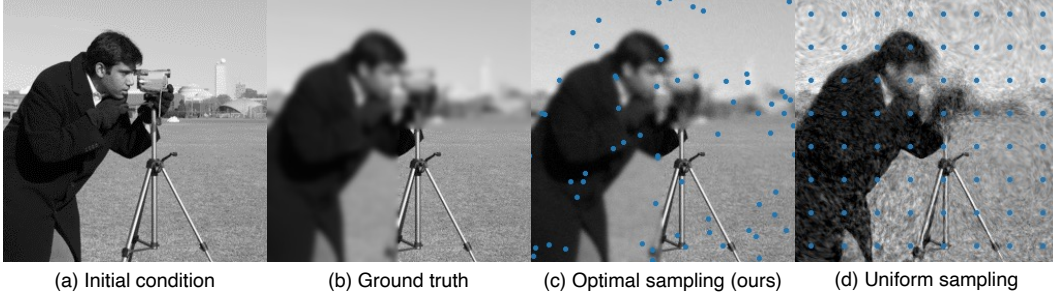


Figure 6: Blurring of portions of the image (20 time steps). (b) Ground truth solution uses all $P = 65,536$ pixels. (c) Our approach uses very few integration samples ($|\mathcal{M}| = 63$, blue circles) and obtains a similar result as the ground truth (PSNR 36.1). (d) Naive uniform sampling ($|\mathcal{M}| = 64$, blue circles) leads to a poor agreement with the ground truth (PSNR 23.4).

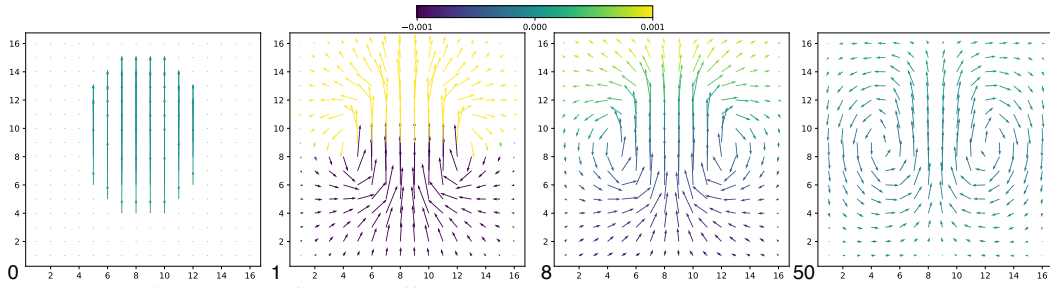


Figure 7: 2D fluid velocity fields at different time steps (0, 1, 8, 50). The velocity vectors are colored by the pressure values. Due to incompressibility, the initial vertical velocity field turns into two vortices.

Solid Mechanics $\rho_0 \ddot{\phi} = \nabla \cdot P(\nabla \phi) + \rho_0 B$ Our approach can also solve the second-order elastodynamics equation for the deformation map ϕ of soft bodies, where ρ_0 is the initial density, P is the first Piola–Kirchhoff stress, and B is the body force density. Figures 8 and 9 demonstrate CROM’s ability to efficiently simulate large deformations.

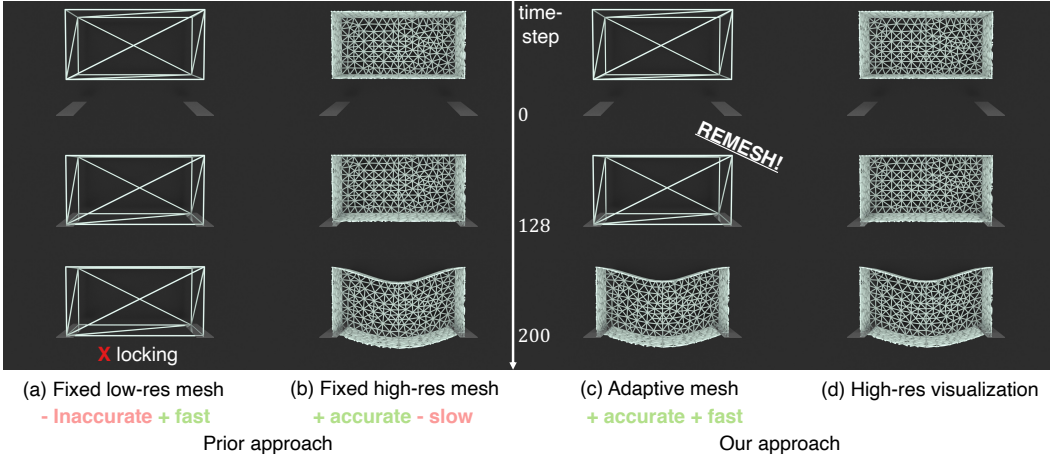


Figure 8: Solid mechanics: adaptive discretization. Due to gravity, a volumetric deformable body falls vertically and impacts two static objects. (a and b) Prior approaches only support reduced-order simulations with fixed discretizations. Therefore, they face a dilemma between accuracy and computation cost. (c) Our approach optimally balances the accuracy and the cost via adaptively changing the computation mesh. (d) Independent of the discretization used in the simulation, our approach can always visualize the result in high-resolution (or any resolution) by invoking the infinite-resolution implicit neural representation.

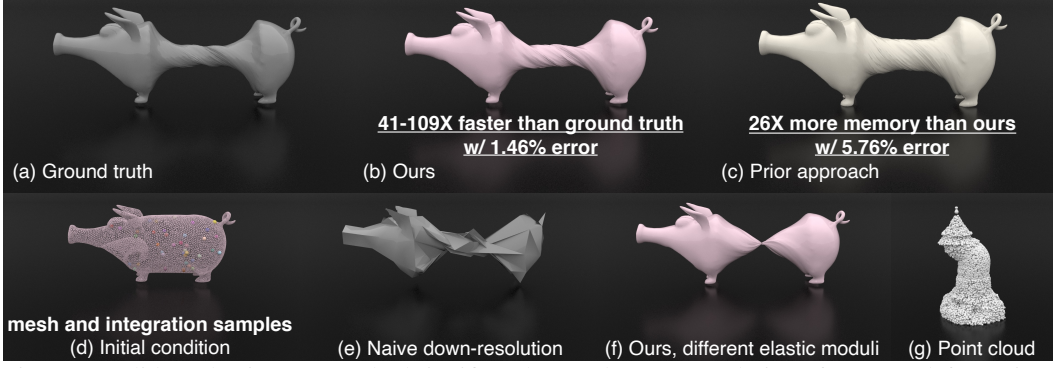


Figure 9: Solid mechanics: our method significantly speeds up PDE solution of extreme deformations. (a) The ground truth is generated via the full-order PDE solver. (b) Our approach is $41\text{-}109\times$ faster than the ground truth while capturing detailed shearing and volume-preserving behaviors (1.46% error). (c) Prior approach (specifically, POD) of the same latent space dimension consumes $26\times$ more memory while suffering from volume-gain artifacts (5.76% error). (d) These simulations adopt a tetrahedral discretization (d, pink mesh, $P = 66, 608$). Instead of using the expensive high-resolution mesh, our approach computes dynamics using very few integration samples (d, colorful spheres, $|\mathcal{M}| = 40$). (e) Naive down-resolution of the ground truth simulation yields a similar runtime but leads to significantly worse quality. (f) After training, our model can capture a wide range of material properties. (g) The same low-dimensional manifold architecture (different network weights) can also be used for model-reducing point-cloud based simulation (reproduced from the work by (Chen et al., 2021)). Disclaimer: the authors do not support animal cruelty.

5.1 Comparisons

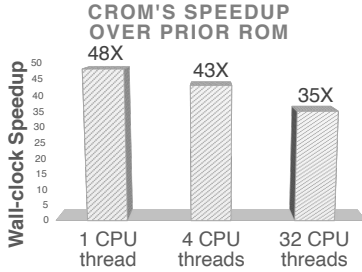


Figure 10: Our speedup advantage is most noticeable with limited computation resources, i.e., 1 CPU thread.

employ a low-quality mesh ($P = 8$ vertices) to economize computation (Figure 8c). When the material collides, we effortlessly switch to a high-quality mesh ($P = 2,065$) for detailed contact resolution (Figure 8c). Figure 10 reports the speedup advantage by optimally adapting the discretization resolution alone. No spatial sample reduction technique (Section 4.4) is applied, i.e., $|\mathcal{M}| = P$. Spatial sample reduction techniques (An et al., 2008) may also be used to alternatively accelerate the high-resolution mesh simulation.

Furthermore, since prior model reduction approaches' low-dimensional manifold is discretization-dependent, the more discretized spatial samples (P) used, the higher the memory consumption of the low-dimensional manifold. By contrast, our model reduction approach is discretization-independent and therefore memory-agnostic with respect to the number of discretized samples. Compared to POD with the same latent space dimension (Figure 9c, $P = 66, 608$, 5.76% error), our approach uses $26\times$ less memory while capturing the ground truth deformation more closely, both qualitatively (better volume preservation) and quantitatively (1.46% error).

Since CROM is not constructed for a fixed discretization, we can adopt an identical low-dimensional manifold architecture (with different weights) to model-reduce simulations of both tetrahedral meshes and point clouds (see Figure 9g). Notably, prior discretization-dependent model reduction approaches are not compatible with point cloud simulations due to the lack of information about gradients and

Comparison with Prior Approaches We specifically compare our method with proper orthogonal decomposition (POD) (Berkooz et al., 1993) but note that the comparisons are fundamental in nature and generalize to other prior discretization-dependent ROM approaches.

Prior methods (see Figure 1a) are obliged to use a fixed discretization throughout the PDE solving. Consider the experiment presented in Figure 8: prior discretization-dependent approaches have to use the high-resolution mesh in order to capture accurate results (Figure 8a and b). Because our approach is discretization-agnostic, we optimally adapt the discretization throughout latent space dynamics. Initially, the material falls and experiences minimal deformation, so we

degrees of freedom outside the training set (Chen et al., 2021). Moreover, even though these examples (Figures 8 and 9) leverage completely different meshes, they use the same network architecture (with different weights), which is also impossible with prior approaches.

Comparison with Full-order Model We profile the performance of CROM against the full-order model on CPUs, consumer GPUs, and data center GPUs (see Figure 11) for the experiment from Figure 9. To facilitate fair comparisons, full models and reduced models share the same (parallelized) PDE solver code, and the only difference between them is the neural network evaluation in the reduced model. Because of the spatial sample reduction (from $P = 66,608$ to $|\mathcal{M}| = 40$), our model consistently obtains a significant wall-clock speedup.

More details on comparisons with prior approaches and the full-order model are provided in the supplement.

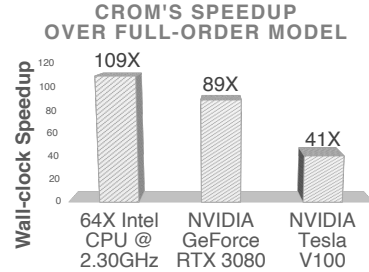


Figure 11: Regardless of compute platform, we obtain significant speedups for the solid mechanics experiment depicted in Figure 9.

6 Discussion and Conclusion

CROM is the *first* discretization-agnostic model reduction framework for PDEs. Disentangling the low-dimensional manifold from the discretization leads to important modeling and computation benefits. These benefits arise primarily from reformulating the reduced manifold as a map accepting not only q but also x as an input; the underlying implementation in terms of neural networks is useful but potentially replaceable, e.g., Yu et al. (2021) implemented NeRF without neural networks. Even so, recent advances in implicit neural representations spurred the realization of CROM. The multilayer perceptron (MLP) architecture drastically simplifies the process of building functions with high-dimensional inputs, which forms the foundation for the latent space construction in this work.

While we offer several advantages over prior model reduction works, we also inherit the limitations of model reduction. Our approach can only handle PDE solutions in the space spanned by the low-dimensional manifold (determined by the training data) and does not generalize to arbitrary unseen scenarios. Such a limitation is also commonly found among other implicit neural representation works (Xie et al., 2021). Future research should consider improving generalizability and data efficiency via meta-learning and integration of stronger priors (Sitzmann et al., 2020a).

Compared to end-to-end ML solutions to PDEs (Sanchez-Gonzalez et al., 2020), CROM employs the neural network strictly as a spatial representation (see Sections 4.1 and 4.3) and solves the PDE using classical PDE-integration numerical methods (see Section 4.2). As such, we believe CROM will open doors for more forthcoming hybrid ML-PDE solutions. As shown in our work, these solutions enforce physical laws (see Figure 5), allow for easy integration with existing PDE solvers (see Section 4.2), and obtain practical computational savings that can be directly employed in production (see Figure 9).

While all training data presented in this work come from classical numerical solvers (e.g., finite element method), CROM is solver-agnostic. At its heart, CROM is a general dimension-reduction technique for spatiotemporal series. Recent ML-based PDE solvers such as PINN, GNN, or long short-term memory (LSTM) networks can also benefit from CROM’s dimension and spatial sample reduction ability.

Societal Impact CROM contributes to the broader effort of solving PDEs quickly. Interactive-rate solutions of PDEs have applications spanning computer-aided design (interactive-rate evaluation and visualization of engineering/product/architectural designs) and medical procedure planning; real-time solutions of PDEs have applications to robotics (including autonomous driving), computer games, and virtual and augmented reality. All of these application areas require careful ethical consideration of their utilization, e.g., to replace human workers with technology, to build-in security backdoors, to develop weapons, and to doctor images.

Acknowledgments and Disclosure of Funding

This work was supported in part by the National Science Foundation (Grants CBET-17-06689) and SideFX. We thank Honglin Chen and Rundi Wu for their insightful discussions. We thank Rundi Wu

for sharing his implementation of Stable Fluids. We thank Raymond Yun Fei for rendering advice. We thank Keenan Crane for the "Origins of the Pig" mesh.

References

- An, S.S., Kim, T., James, D.L., 2008. Optimizing cubature for efficient integration of subspace deformations. *ACM transactions on graphics (TOG)* 27, 1–10.
- Bai, Z., 2002. Krylov subspace techniques for reduced-order modeling of large-scale dynamical systems. *Applied numerical mathematics* 43, 9–44.
- Barbič, J., James, D.L., 2005. Real-time subspace integration for st. venant-kirchhoff deformable models. *ACM transactions on graphics (TOG)* 24, 982–990.
- Benner, P., Gugercin, S., Willcox, K., 2015. A survey of projection-based model reduction methods for parametric dynamical systems. *SIAM review* 57, 483–531.
- Berkooz, G., Holmes, P., Lumley, J.L., 1993. The proper orthogonal decomposition in the analysis of turbulent flows. *Annual review of fluid mechanics* 25, 539–575.
- Carlberg, K.T., 2011. Model reduction of nonlinear mechanical systems via optimal projection and tensor approximation. Ph.D. thesis. Stanford University.
- Chen, P.Y., Chiaramonte, M., Grinspun, E., Carlberg, K., 2021. Model reduction for the material point method via an implicit neural representation of the deformation map. *arXiv preprint arXiv:2109.12390*.
- Chen, Z., Zhang, H., 2019. Learning implicit fields for generative shape modeling, in: *Proceedings of the IEEE/CVF Conference on Computer Vision and Pattern Recognition*, pp. 5939–5948.
- Dormand, J.R., Prince, P.J., 1980. A family of embedded runge-kutta formulae. *Journal of computational and applied mathematics* 6, 19–26.
- Fulton, L., Modi, V., Duvenaud, D., Levin, D.I., Jacobson, A., 2019. Latent-space dynamics for reduced deformable simulation, in: *Computer graphics forum*, Wiley Online Library. pp. 379–391.
- Hughes, T.J., 2012. *The finite element method: linear static and dynamic finite element analysis*. Courier Corporation.
- Kim, B., Azevedo, V.C., Thuerey, N., Kim, T., Gross, M., Solenthaler, B., 2019. Deep fluids: A generative network for parameterized fluid simulations, in: *Computer Graphics Forum*, Wiley Online Library. pp. 59–70.
- Lee, K., Carlberg, K.T., 2020. Model reduction of dynamical systems on nonlinear manifolds using deep convolutional autoencoders. *Journal of Computational Physics* 404, 108973.
- Lumley, J.L., 1967. The structure of inhomogeneous turbulent flows. *Atmospheric turbulence and radio wave propagation*.
- Mescheder, L., Oechsle, M., Niemeyer, M., Nowozin, S., Geiger, A., 2019. Occupancy networks: Learning 3d reconstruction in function space, in: *Proceedings of the IEEE/CVF Conference on Computer Vision and Pattern Recognition*, pp. 4460–4470.
- Mildenhall, B., Srinivasan, P.P., Tancik, M., Barron, J.T., Ramamoorthi, R., Ng, R., 2020. Nerf: Representing scenes as neural radiance fields for view synthesis, in: *European conference on computer vision*, Springer. pp. 405–421.
- Moore, B., 1981. Principal component analysis in linear systems: Controllability, observability, and model reduction. *IEEE transactions on automatic control* 26, 17–32.
- Nocedal, J., Wright, S., 2006. *Numerical optimization*. Springer Science & Business Media.
- Pan, S., Brunton, S.L., Kutz, J.N., 2022. Neural implicit flow: a mesh-agnostic dimensionality reduction paradigm of spatio-temporal data. *arXiv preprint arXiv:2204.03216*.
- Park, J.J., Florence, P., Straub, J., Newcombe, R., Lovegrove, S., 2019. DeepSDF: Learning continuous signed distance functions for shape representation, in: *Proceedings of the IEEE/CVF Conference on Computer Vision and Pattern Recognition*, pp. 165–174.

- Perona, P., Malik, J., 1990. Scale-space and edge detection using anisotropic diffusion. *IEEE Transactions on pattern analysis and machine intelligence* 12, 629–639.
- Raissi, M., Perdikaris, P., Karniadakis, G.E., 2019. Physics-informed neural networks: A deep learning framework for solving forward and inverse problems involving nonlinear partial differential equations. *Journal of Computational Physics* 378, 686–707.
- Sanchez-Gonzalez, A., Godwin, J., Pfaff, T., Ying, R., Leskovec, J., Battaglia, P., 2020. Learning to simulate complex physics with graph networks, in: *International Conference on Machine Learning*, PMLR. pp. 8459–8468.
- Shen, S., Yin, Y., Shao, T., Wang, H., Jiang, C., Lan, L., Zhou, K., 2021. High-order differentiable autoencoder for nonlinear model reduction. *arXiv preprint arXiv:2102.11026* .
- Sirovich, L., 1987. Turbulence and the dynamics of coherent structures. i. coherent structures. *Quarterly of applied mathematics* 45, 561–571.
- Sitzmann, V., Chan, E., Tucker, R., Snavely, N., Wetzstein, G., 2020a. Metasdf: Meta-learning signed distance functions. *Advances in Neural Information Processing Systems* 33, 10136–10147.
- Sitzmann, V., Martel, J., Bergman, A., Lindell, D., Wetzstein, G., 2020b. Implicit neural representations with periodic activation functions. *Advances in Neural Information Processing Systems* 33.
- Wiewel, S., Becher, M., Thuerey, N., 2019. Latent space physics: Towards learning the temporal evolution of fluid flow, in: *Computer graphics forum*, Wiley Online Library. pp. 71–82.
- Willcox, K., Peraire, J., 2002. Balanced model reduction via the proper orthogonal decomposition. *AIAA journal* 40, 2323–2330.
- Xie, Y., Takikawa, T., Saito, S., Litany, O., Yan, S., Khan, N., Tombari, F., Tompkin, J., Sitzmann, V., Sridhar, S., 2021. Neural fields in visual computing and beyond. *arXiv preprint arXiv:2111.11426* .
- Yu, A., Fridovich-Keil, S., Tancik, M., Chen, Q., Recht, B., Kanazawa, A., 2021. Plenoxels: Radiance fields without neural networks. *arXiv preprint arXiv:2112.05131* .

CROM: Continuous Reduced-Order Modeling of PDEs Using Implicit Neural Representations – Supplementary Material –

Peter Yichen Chen¹

Jinxu Xiang¹

Dong Heon Cho¹

G A Pershing¹

Henrique Teles Maia¹

Maurizio Chiaramonte²

Kevin Carlberg²

Eitan Grinspun^{3,1}

¹Columbia University

²Meta Reality Labs Research

³University of Toronto

We highly encourage viewing the **supplementary video** where our results are best illustrated.

Contents

1	Optimal Sampling	3
2	Network Inversion	4
2.1	Initial Guess for the Nonlinear Solver	4
2.2	Linearization	4
3	Network Details	5
3.1	Training Details	5
4	Network Gradients	5
4.1	Network Gradients via Direct Differentiation	6
4.1.1	Efficient Implementation	6
4.1.2	Failure Modes	6
4.2	Network Gradients via Numerical Differentiation	6
5	Hyperparameters	7
6	Thermodynamics	9
6.1	Continuous PDE	9
6.2	Full-order Model	9
6.3	Reduced-order Model	9
6.4	Training and Testing Data	10
6.5	Results	10
7	Image Processing	11
7.1	Continuous PDE	11
7.2	Full-order Model	11
7.3	Reduced-order Model	11
7.4	Training and Testing Data	11
7.5	Results	11
8	Fluid Dynamics	12
8.1	Continuous PDE	12
8.2	Full-order Model	12
8.3	Reduced-order Model	12
8.4	Training and Testing Data	13
8.5	Results	13
9	Solid Mechanics	13
9.1	Continuous PDE	13
9.2	Full-order Model	14

9.3	Reduced-order Model	14
9.4	Training and Testing Data	14
9.4.1	Gravity-induced Impact	14
9.4.2	Torsion and Tension	15
9.5	Results	15
10	Comparison with Prior Approaches	15
10.1	Speed	16
10.2	Memory	16
10.3	Accuracy	16
11	Comparison with the Full-order Model	17

1 Optimal Sampling

To select the integration samples optimally, we aim to balance the computation speed and accuracy. CROM employs $|\mathcal{M}|$ spatial samples, and the computation speed roughly scales linearly with the number of samples. To maximize computation speed, we aspire to select the fewest number of samples possible.

Given a target accuracy, our greedy algorithm selects the fewest number of integration samples from the discrete samples $\{\mathbf{x}^i\}_{i=1}^P$ of the full-order PDE solution in order to achieve the target accuracy.

Algorithm 1: Optimal sampling

```

1  $\mathcal{M} = \{\mathbf{x}^k\}$  // randomly initialize integration sample set,  $k \in \{1, \dots, P\}$ 
2 while true do
3    $res\_vec = Calculate\_Residual(\mathcal{M})$ 
4   if  $Metric(res\_vec) < target\_accuracy$  then
5     return  $\mathcal{M}$ 
6   else
7      $indices = Max\_Indices(res\_vec, \mathcal{Q})$  // find  $\mathcal{Q}$  indices with the largest individual
      residuals
8      $res\_list = \mathbf{0} \in \mathbb{R}^{\mathcal{Q}}$ 
9     for  $i$  in  $indices$  do
10       $res\_list[i] = Metric(Calculate\_Residual(\mathcal{M} \cup \{\mathbf{x}^i\}))$ 
11    end
12     $j = Min\_Indices(res\_list, 1)$  // find the index with the smallest global residual
13     $\mathcal{M} = \mathcal{M} \cup \{\mathbf{x}^j\}$ 
14  end
15 end
16 Function  $Calculate\_Residual(\mathcal{M})$ :
17    $res\_vec = \mathbf{0} \in \mathbb{R}^P$ 
18   for  $\mu \in \mathcal{D}_{train}$  do
19     Obtain the final latent space vector  $\mathbf{q}(t_T; \mu)$  with the integration samples ( $\mathcal{M}$ )
20     for  $i = 1, \dots, P$  do
21        $res\_vec[i] += \|g_{\theta_g}(\mathbf{x}^i, \mathbf{q}(t_T; \mu)) - \mathbf{f}(\mathbf{x}^i, t_T)\|$ 
22     end
23   end
24   return  $res\_vec$ 
25 Function  $Metric(res\_vec)$ :
26   return  $mean(res\_vec) + max(res\_vec)$ 

```

In every iteration, the greedy algorithm adds one spatial sample to the sample set \mathcal{M} and lowers the error of latent space dynamics. Specifically, the algorithm loops over Q spatial samples with the largest individual residuals. We test adding each sample to the integration sample set and compute a new global residual. From these Q samples, we select the one leading to the smallest new global residual and add it to the actual sample set. The algorithm repeats until the target accuracy is met. In practice, we find $Q = 10$ gives sufficient results. Algorithm 1 describes the details. Compared to the naive uniform sampling approach, our optimal sampling scheme yields significantly more accurate results (see Figure 4 in the main text).

2 Network Inversion

In order to generate latent space dynamics, we need to invert the neural network employed for the low-dimensional manifold. We do so by solving the minimization problem:

$$\min_{\mathbf{q}_{n+1} \in \mathbb{R}^r} \sum_{\mathbf{y} \in \mathcal{M}} \|\mathbf{g}_{\theta_g}(\mathbf{y}, \mathbf{q}_{n+1}) - \mathbf{f}(\mathbf{y}, t_{n+1})\|_2^2.$$

Since this is a nonlinear least-squares problem, we solve it with the classic iterative Gauss-Newton algorithm (Nocedal and Wright, 2006). Unlike Newton’s method, Gauss-Newton does not require the Hessian of the objective function. Consequently, in addition to the neural network itself, we only need to evaluate the gradient of the neural network with respect to the latent space vector $\frac{\partial \mathbf{g}_{\theta_g}}{\partial \mathbf{q}}(\mathbf{y}, \mathbf{q}_{n+1})$. We also equip our Gauss-Newton implementation with a standard backtracking line-search scheme to improve the convergence rate.

2.1 Initial Guess for the Nonlinear Solver

An initial guess close to the minimum is necessary for the convergence of Gauss-Newton. The previous time step latent space vector \mathbf{q}_n serves as an ideal initial guess since \mathbf{f} does not vary much over a time step. However, in the extreme cases where \mathbf{f} deviates significantly over one time step, we find it helpful to compute the initial guess through an encoder network. For convenience, we employ the encoder network from training, which requires computing the dynamics for P samples. Since these extreme cases are rare (e.g., the first two time steps of an operator-splitting-based fluid solver where a large change in pressure is necessary for enforcing incompressibility), the computation overhead over a fully $|\mathcal{M}|$ treatment is minimal. Future work should consider building this encoder network strictly for the degrees of freedom in \mathcal{M} . We can further facilitate nonlinear solver convergence by improving the latent space quality, such as employing a Jacobian penalty term (Chen et al., 2021) / local isometry term (Du et al., 2021) and enforcing Lipschitz constraints (Liu et al., 2022).

2.2 Linearization

We can further obtain computation-save by bypassing the iterative nonlinear solver and linearizing the least-squares problem.

We define $\Delta \mathbf{f}$ as,

$$\begin{aligned} \Delta \mathbf{f}(\mathbf{y}, t_{n+1}) &= \mathbf{f}(\mathbf{y}, t_{n+1}) - \mathbf{f}(\mathbf{y}, t_n) \\ &= \mathbf{f}(\mathbf{y}, t_{n+1}) - \mathbf{g}_{\theta_g}(\mathbf{y}, \mathbf{q}_n). \end{aligned}$$

Employing Taylor expansion of \mathbf{g}_{θ_g} at \mathbf{q}_n , we have $\mathbf{g}_{\theta_g}(\mathbf{y}, \mathbf{q}_{n+1}) \approx \mathbf{g}_{\theta_g}(\mathbf{y}, \mathbf{q}_n) + \frac{\partial \mathbf{g}_{\theta_g}}{\partial \mathbf{q}}(\mathbf{y}, \mathbf{q}_n) \Delta \mathbf{q}_{n+1}$, where $\mathbf{q}_{n+1} = \mathbf{q}_n + \Delta \mathbf{q}_{n+1}$. Therefore, the original objective function can be approximated as,

$$\begin{aligned} \mathbf{g}_{\theta_g}(\mathbf{y}, \mathbf{q}_{n+1}) - \mathbf{f}(\mathbf{y}, t_{n+1}) &= \mathbf{g}_{\theta_g}(\mathbf{y}, \mathbf{q}_{n+1}) - \mathbf{g}_{\theta_g}(\mathbf{y}, \mathbf{q}_n) - \Delta \mathbf{f}(\mathbf{y}, t_{n+1}) \\ &\approx \frac{\partial \mathbf{g}_{\theta_g}}{\partial \mathbf{q}}(\mathbf{y}, \mathbf{q}_n) \Delta \mathbf{q}_{n+1} - \Delta \mathbf{f}(\mathbf{y}, t_{n+1}). \end{aligned}$$

Therefore, we can obtain the latent space dynamics by solving the *linear* least-squares problem,

$$\min_{\Delta \mathbf{q}_{n+1} \in \mathbb{R}^r} \sum_{\mathbf{y} \in \mathcal{M}} \left\| \frac{\partial \mathbf{g}_{\theta_g}}{\partial \mathbf{q}}(\mathbf{y}, \mathbf{q}_n) \Delta \mathbf{q}_{n+1} - \Delta \mathbf{f}(\mathbf{y}, t_{n+1}) \right\|_2^2.$$

This is the normal equation and can be solved in the closed form:

$$\Delta \mathbf{q}_{n+1} = (\mathbf{J}^T \mathbf{J})^{-1} \mathbf{J}^T \mathbf{b},$$

where \mathbf{J} is the $(|\mathcal{M}| \cdot d)$ by r Jacobian matrix that contains $\frac{\partial \mathbf{g}_{\theta_g}}{\partial \mathbf{q}}(\mathbf{y}, \mathbf{q}_n), \forall \mathbf{y} \in \mathcal{M}$; \mathbf{b} is the $(|\mathcal{M}| \cdot d)$ by 1 residual vector containing $\Delta \mathbf{f}(\mathbf{y}, t_{n+1}), \forall \mathbf{y} \in \mathcal{M}$.

Since our work features both small $|\mathcal{M}|$ and small r , the closed-form network inversion costs just a few small dense matrix multiplications and thereby introduces minimal overhead. In fact, the solver itself is extremely efficient, and the majority of the computation cost is forming the Jacobian matrix \mathbf{J} itself, whose optimization will be discussed in Section 4.1.1. Additional performance details are listed in Section 11.

3 Network Details

Consistent with the implicit neural representation literature, we parameterize the low-dimensional manifold with an MLP network \mathbf{g}_{θ_g} . The input dimension of the network is $m + r$ while the output dimension of the network is d , where m is the dimension of the input spatial vector while d is the output dimension of the vector field of interest. Our MLP network contains 5 hidden layers, each of which has a width of $(\beta \cdot d)$, where β is the hyperparameter that defines the learning capacity of the network. Essentially, our network has two tunable hyperparameters, r and β . A detailed study on these hyperparameters will be discussed in Section 5.

Since we require the network to be continuously differentiable with respect to both the spatial coordinates \mathbf{x} and the latent space vector \mathbf{q} , we adopt continuously differentiable activation functions. In practice, either ELU (Clevert et al., 2015) or SIREN (Sitzmann et al., 2020) serves the purpose.

For the encoder network \mathbf{e}_{θ_e} , the input is a 1D vector of length P with d channels. The output is a vector of dimension r . Using MLPs would lead to enormous network size when P is large. We therefore design an encoder network first to apply multiple 1D convolution layers of kernel size 6, stride size 4, and output channel size d until the output 1D vector’s length is the closest to $32/d$ but no smaller. Afterward, the encoder network reshapes the vector into 1 channel and applies an MLP layer to reduce the dimension of the vector to 32. The last MLP layer then transforms the previous 32-dimensional vector into dimension r . Discretization-specific encoder networks can also be used, e.g., PointNet for point clouds and convolutional neural network for grid data.

3.1 Training Details

We use the Adam optimizer (Kingma and Ba, 2014) for stochastic gradient descent. We use the Xavier initialization for ELU layers and the default initialization ($\omega_0 = 30$) for SIREN layers. Unless otherwise noted, we train with a base learning rate of $lr = 1e - 4$ and adopt a learning rate decay strategy ($10 \cdot lr \rightarrow 5 \cdot lr \rightarrow 2 \cdot lr \rightarrow 1 \cdot lr \rightarrow 0.5 \cdot lr \rightarrow 0.2 \cdot lr$). For each aforementioned learning rate, we train for 30,000 epochs. We adopt a batch size 16 (i.e., 16 simulation snapshots) for the encoder and therefore a batch size of $16 \cdot P$ for the implicit-neural-representation-based low-dimensional manifold. We implement the entire training pipeline in PyTorch Lightning (Falcon et al., 2019) which facilitates distributed training across multiple GPUs. The training vector fields are standardized to have zero mean and unit variance. The training spatial coordinates are also standardized for the ELU implementation, but they are preprocessed to be between $[-1, 1]$ for the SIREN implementation.

4 Network Gradients

Gradients of the implicit neural representation ($\nabla_{\mathbf{x}} \mathbf{g}_{\theta_g}$ and $\frac{\partial \mathbf{g}_{\theta_g}}{\partial \mathbf{q}}$) are crucial for our reduced-order pipeline. We use them to compute the spatial and temporal gradients of the vector fields,

$\nabla f(x, t) = \nabla_x g_{\theta_g}(x, q)$ and $\dot{f}(x, t) = \frac{\partial g_{\theta_g}}{\partial q}(x, q)\dot{q}$. Furthermore, the gradient with respect to the latent space $\frac{\partial g_{\theta_g}}{\partial q}$ is also a key ingredient for the network inversion (Section 2).

4.1 Network Gradients via Direct Differentiation

One way to compute the gradients is through directly differentiating the continuously differentiable network.

4.1.1 Efficient Implementation

Algorithm 2: Network gradient

Input: x

Output: $\frac{\partial g_{\theta_g}}{\partial x}(x), g_{\theta_g}(x)$

- 1 Let $g_{\theta_g} = g_n \circ \dots \circ g_1$ be a n -layer MLP network of interest.
 - 2 Initialization: $\frac{\partial y}{\partial x} = I, y = x$
 - 3 **for** $i = 1, \dots, n$ **do**
 - 4 $\frac{\partial y}{\partial x} = \frac{\partial g_i}{\partial x}(y) \frac{\partial y}{\partial x}$
 - 5 $y = g_i(y)$
 - 6 **end**
 - 7 **return** $\frac{\partial y}{\partial x}, y$
-

Unfortunately, computing these differentiations via auto-diff (computational graph tracking) is too slow for the high-performance application explored in this work. To ensure maximum efficiency, we implement the gradients analytically through the chain rules of each network layer. Since we only use fully-connected layers, the implementation is straightforward. In addition, along the way of computing the gradient via chain rules, we also obtain the function value of the neural network itself. Therefore, we obtain both the gradient and the function value in a single forward pass. Algorithm 2 describes the details.

4.1.2 Failure Modes

While direct differentiation is generally accurate, we observe failure modes when the training samples are sparse. Consider the case where $g_{\theta_g}(x, q) = x$, e.g., the undeformed, reference configuration of elastodynamics. In this case, the ground truth spatial gradient is $\nabla_x g_{\theta_g} = I$.

We train the neural network with spatial samples discussed in Section 9.4.1. After training, we evaluate the spatial gradients at the center of each tetrahedron and compute its error (from the identity matrix) in the L2 norm. As shown in Figure 1, errors are observed in both ELU and SIREN networks while SIREN’s error is significantly larger, c.f., (Yang et al., 2021). This discrepancy can be understood as the high-frequency prior by SIREN is more suitable for approximating high-frequency functions. By contrast, the low-frequency prior by ELU is better at approximating low-frequency functions (Hertz et al., 2021).

We find training with more samples and/or gradient supervision (Chen et al., 2021) reduces the errors above at the cost of additional training resources but does not resolve the issue completely.

4.2 Network Gradients via Numerical Differentiation

Another approach to computing neural network gradients is numerical approximation, such as the finite difference method and the finite element method. Figure 1 demonstrates the drastically improved gradient accuracy with the finite element method (linear basis function) on networks trained with SIREN. We find such a hybrid approach to be an ideal middle ground, i.e., we represent the function itself with the discretization-independent neural network and compute the gradient via discretization-dependent numerical differentiation.

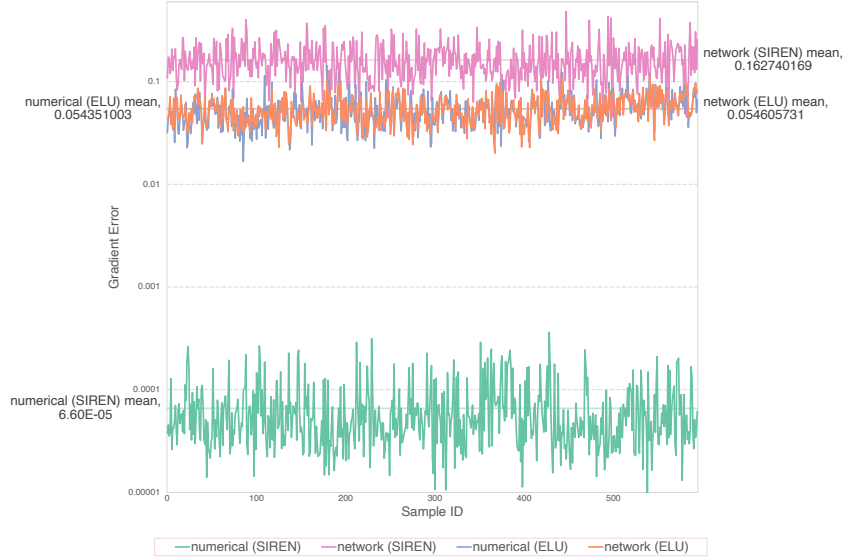


Figure 1: Gradient errors evaluated at the centers of tetrahedra. Numerical differentiation (specifically, finite element with linear basis) significantly improves the gradient accuracy of SIREN.

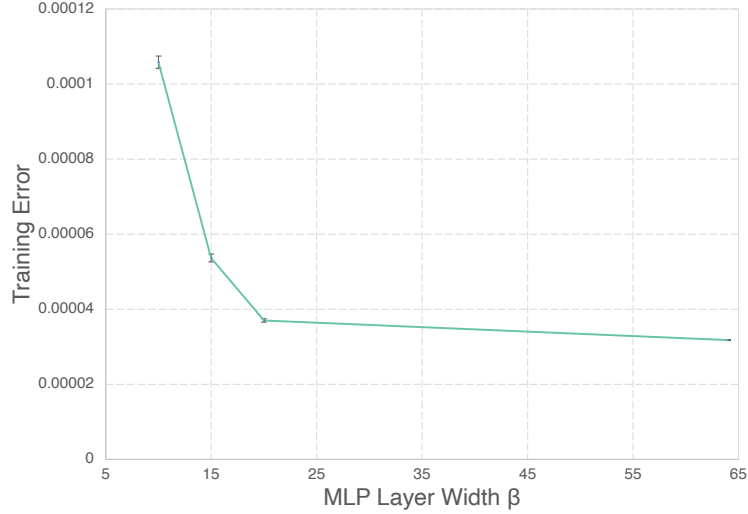


Figure 2: Training accuracy vs. the MLP layer width (β). For each setup, we repeat the training for 8 times. The mean values and the error bars are shown. Increasing MLP layer width leads to higher accuracy.

5 Hyperparameters

During the offline training stage, we can modify two network architecture hyperparameters: the size of the latent space (r) and the width of the MLP (β). After training and during the online deployment stage of the model, the key hyperparameter is the number of integration samples ($|\mathcal{M}|$). In this section, we run a sensitivity analysis on these hyperparameters.

Figure 2 shows that increasing the width of each MLP layer improves the training accuracy. Unless otherwise noticed, all training errors reported are mean squared errors (MSE).

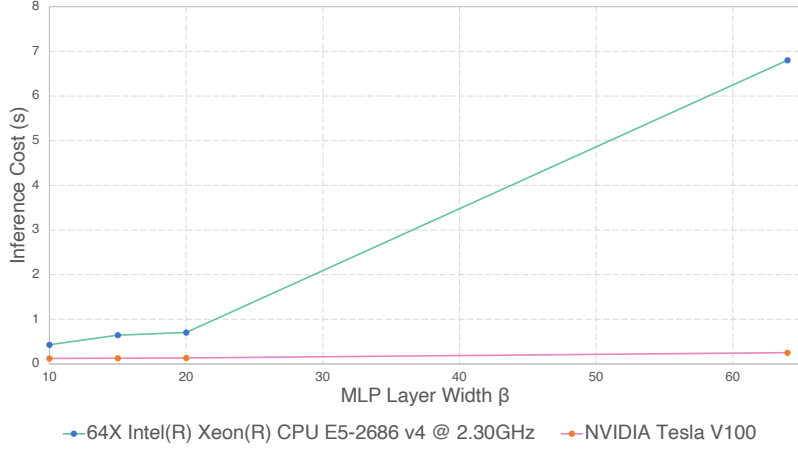


Figure 3: Network inference cost (CPU and GPU) vs. the MLP layer width (β). Inference cost (over 100 runs) increases as the network size increases. CPU suffers from a more severe performance drop than GPU.

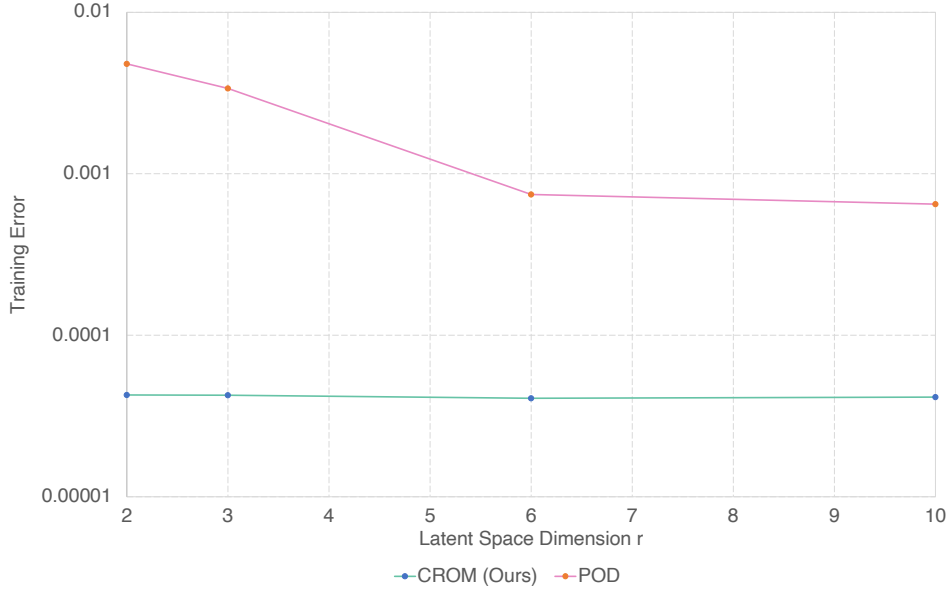


Figure 4: Training accuracy vs. latent space vector dimension r . Our CROM is orders-of-magnitude more accurate than POD across different latent space dimensions. Unlike POD, our approach’s accuracy does not increase with the latent space dimension.

However, large layer widths also entail higher computational cost (see Figure 3). Compared to the highly parallelized GPUs, CPUs suffer from a more severe performance drop due to the larger network size.

Unlike traditional PCA-based model reduction approaches (e.g., POD), increasing the dimension of the latent space vector does not yield higher accuracy for our approach (see Figure 4). In prior ROM approaches, augmenting the dimension of the latent space vector directly increases the number of entries in the low-dimensional manifold matrix, which, in turn, improves the approximation capacity of the low-dimensional manifold. However, as shown in Figure 2, in the implicit neural representation framework, we can control the learning capacity of the network architecture by explicitly modifying the width of the MLP layer. Therefore, the importance of the latent space dimension diminishes.

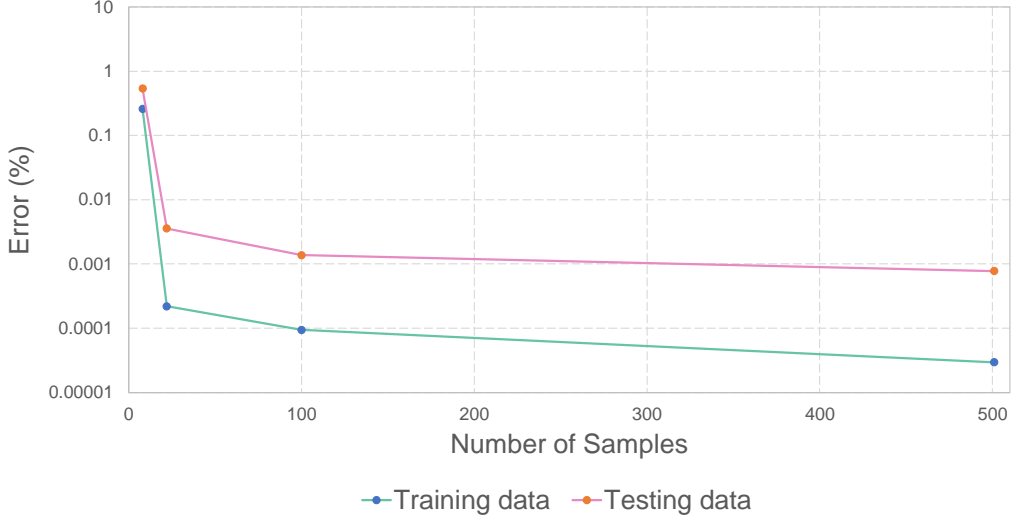


Figure 5: PDE solution accuracy vs. the number of samples. Increasing integration sample counts yields higher accuracies on both training and testing data.

During the online stage of the reduced-order model, we select integration samples via the greedy-based optimal sampling scheme (Section 1). Increasing the number of integration samples leads to higher accuracy (Figure 5).

6 Thermodynamics

6.1 Continuous PDE

$$\frac{\partial u}{\partial t} - \nu(x) \frac{\partial^2 u}{\partial x^2} = 0$$

In thermodynamics, we study the 1D heat equation of the spatiotemporal dependent temperature u . We assume a zero-Dirichlet boundary condition, though other boundary conditions can also be incorporated.

6.2 Full-order Model

The full-order model discretizes the spatial vector field with a regular Eulerian grid using 501 equally spaced samples ($P = 501$).

We then approximate the spatial gradient using the finite difference method,

$$\frac{\partial^2 u}{\partial x^2}(x^i, t_n) = \frac{u(x^i - \Delta x, t_n) + u(x^i + \Delta x, t_n) - 2u(x^i, t_n)}{\Delta x^2},$$

where Δx is the grid spacing.

We assume a first-order explicit time-stepping scheme,

$$u_{n+1}^i = u_n^i + \Delta t \nu(x^i) \frac{\partial^2 u}{\partial x^2}(x^i, t_n).$$

6.3 Reduced-order Model

Instead of a finite-difference treatment of the spatial gradient, we compute the gradient via direct differentiation of the network. The latent space dimension is $r = 16$ and the width of the MLP is $\beta = 128$.

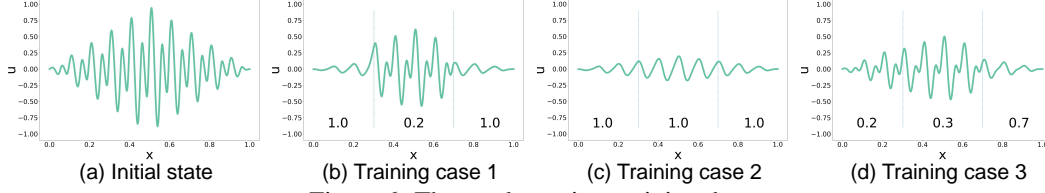


Figure 6: Thermodynamics: training data.

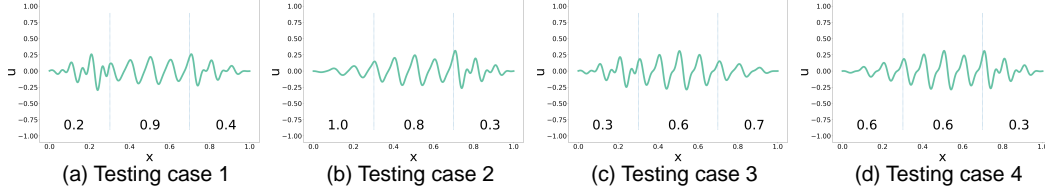


Figure 7: Thermodynamics: reduced-order simulation on the testing dataset.

6.4 Training and Testing Data

We generate training data by setting ν to different piecewise constant functions of three regions, i.e., the parameter vector $\mu \in \mathcal{D} = [0.2, 1.0]^3 \subset \mathbb{R}^3$. Figure 6 displays the initial and the final states of training data. Notice how different regions diffuse with different speeds due to the spatially varying ν . In total, 8 PDE temporal sequences (of 100 time steps) with different ν 's are generated for training. We sample another 4 ν 's for testing purposes.

6.5 Results

Figure 7 demonstrates the performance of the reduced-order model on the testing dataset. With the optimal sampling scheme, we can achieve 0.43% error using just 22 spatial samples (see Figure 4 in the main text). Our approach also supports training and testing with different initial conditions (see Figure 8).

To gauge our approach's ability to conserve physical laws, we measure the energy evolution over time in the region between $x_1 = 0.396$ and $x_2 = 0.526$ (Figure 7). As shown by Cannon (1984), the escaped energy (EE) is measured by the flux difference $(\frac{\partial u}{\partial x}(x_1, t) - \frac{\partial u}{\partial x}(x_2, t))$ at the left and right boundaries integrated over time; the stored energy (SE) is measured by the heat energy density, proportional to the temperature (u), integrated over space; the total energy (TE) is the sum of the prior two energies, i.e., $TE=EE+SE$. Figure 5 in the main text demonstrates that the reduced simulation preserves the total energy over time.

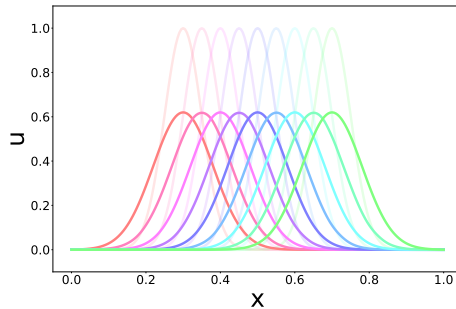


Figure 8: Our reduced-order diffusion solver with various initial conditions (transparent) and the final diffused states. Different colors correspond to different initial conditions.

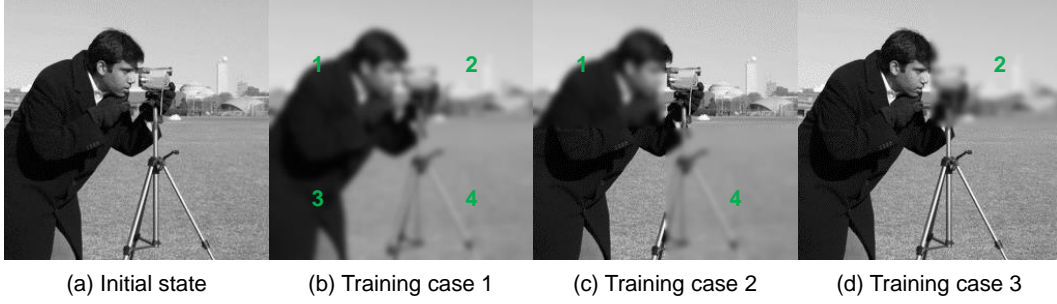


Figure 9: Image Processing: training dataset. The blurred region is numbered.

7 Image Processing

7.1 Continuous PDE

$$\frac{\partial u}{\partial t} - \nu(x) \nabla^2 u = 0$$

In image processing, we study the Perona–Malik diffusion equation of the gray-scale image u (Perona and Malik, 1990).

7.2 Full-order Model

The full-order model discretizes the spatial 2D pixel field with a regular Eulerian grid using 256×256 equally spaced samples ($P = 65,536$).

We then approximate the spatial gradient using the finite difference method,

$$\frac{\partial^2 u}{\partial x^2}(x^i, y^i, t_n) = \frac{u(x^i - \Delta x, y^i, t_n) + u(x^i + \Delta x, y^i, t_n) - 2u(x^i, y^i, t_n)}{\Delta x^2},$$

$$\frac{\partial^2 u}{\partial y^2}(x^i, y^i, t_n) = \frac{u(x^i, y^i - \Delta y, t_n) + u(x^i, y^i + \Delta y, t_n) - 2u(x^i, y^i, t_n)}{\Delta y^2}.$$

We assume a first-order explicit time-stepping scheme,

$$u_{n+1}^i = u_n^i + \Delta t \nu(x^i, y^i) \left(\frac{\partial^2 u}{\partial x^2}(x^i, y^i, t_n) + \frac{\partial^2 u}{\partial y^2}(x^i, y^i, t_n) \right),$$

where $\Delta x = \Delta y$ is the grid spacing.

7.3 Reduced-order Model

The reduced-order model follows the same treatments as Section 6.3.

7.4 Training and Testing Data

Similar to Section 6.4, we generate training data by setting ν to different piecewise constant functions of four equally-spaced regions, i.e., the parameter vector $\mu \in \mathcal{D} = \{0, 0.2\}^4 \subset \mathbb{R}^4$. $\mathcal{D}_{\text{train}}$ contains 11 parameter vectors (Figure 9), where 0, 2 or 3 regions have zero diffusion coefficients, i.e., no blurring. $\mathcal{D}_{\text{test}}$ contains 4 parameter vectors, where only 1 region is unblurred. For each training and testing parameter vector, we run a simulation of 20 time steps.

7.5 Results

Figure 10 demonstrates the reduced simulation's performance on the testing dataset. Furthermore, with the optimal sampling scheme, we can achieve 36.1 PSNR using just 63 spatial samples (see Figure 6 in the main text). The complexity reduction is 99.90%.

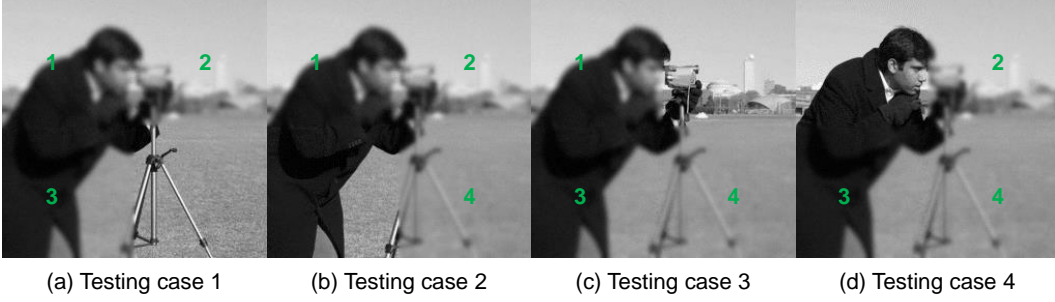


Figure 10: Image Processing: our reduced-order simulation successfully blurs the target regions in the testing dataset. The blurred region is numbered.

8 Fluid Dynamics

8.1 Continuous PDE

$$\frac{\partial \mathbf{u}}{\partial t} + (\mathbf{u} \cdot \nabla) \mathbf{u} = -\nabla p + \nu \nabla^2 \mathbf{u} + \mathbf{f}_{ext}, \quad \nabla \cdot \mathbf{u} = 0$$

We study the incompressible Navier-Stokes equation, where \mathbf{u} is the velocity field, p is the pressure field, and ν is the viscosity. We assume there is no external force, i.e., $\mathbf{f}_{ext} = \mathbf{0}$. We assume a no-penetration boundary condition for the velocity and a zero-Dirichlet boundary condition for the pressure.

8.2 Full-order Model

The full-order model assumes an operator-splitting scheme following the classic Chorin’s projection method (Chorin, 1968). In particular, we follow the implementation by Stam (1999). We summarize the major ingredients and refer to his paper for details.

We sequentially apply 3 linear operators to the velocity field: diffusion, advection, and projection. From the previous time step velocity field \mathbf{u}_n , we apply the diffusion operator according to the viscosity and obtain the diffused velocity $\mathbf{u}_n^{\text{visc}}$. Next, we employ semi-Lagrangian to obtain the advected velocity field $\mathbf{u}_n^{\text{adv}}$. For the last projection step, we first compute the pressure p_{n+1} by solving the poisson equation, $\nabla^2 p_{n+1} = \nabla \cdot \mathbf{u}_n^{\text{adv}}$. Afterwards, we apply the pressure gradient to obtain the divergence-free velocity \mathbf{u}_{n+1} . All operations are done on a 2D 16 by 16 Eulerian grid.

8.3 Reduced-order Model

We compute latent space dynamics (\mathbf{q}_{n+1}) of the velocity field by projecting \mathbf{u}_{n+1} onto the low-dimensional manifold \mathbf{g}_{θ_g} . Furthermore, we train another implicit neural representation based low-dimensional manifold for the pressure field, $h_{\theta_h} \approx p$. Low-dimensional manifold h_{θ_h} evolves a separate latent space vector \mathbf{z} .

One way to compute the latent space dynamics of h_{θ_h} is inverting the network from p_{n+1} :

$$\min_{\mathbf{z}_{n+1} \in \mathbb{R}^r} \sum_{\mathbf{y} \in \mathcal{M}} \|h_{\theta_h}(\mathbf{y}, \mathbf{z}_{n+1}) - p(\mathbf{y}, t_{n+1})\|_2^2. \quad (1)$$

This approach requires obtaining the Poisson-solved pressure p_{n+1} ($\forall \mathbf{y} \in \mathcal{M}$). However, the Poisson solve itself is a global solve and therefore requires all the degrees of freedom (P).

To alleviate this computation burden, we bypass the grid-based Poisson solve and directly invert the network with the divergence-free loss function:

$$\min_{\mathbf{z}_{n+1} \in \mathbb{R}^r} \sum_{\mathbf{y} \in \mathcal{M}} \|\nabla^2 h_{\theta_h}(\mathbf{y}, \mathbf{z}_{n+1}) - \nabla \cdot \mathbf{u}_n^{\text{adv}}\|_2^2. \quad (2)$$

As such, the latent space dynamics of the pressure field now only require spatial samples in \mathcal{M} .

In practice, for the first two time steps of the solver where extreme pressure change happens, we use the first approach (Equation (1)) so that we can benefit from the encoder-based initial guess discussed in Section 2.1. For all remaining time steps, we solve the more efficient Equation (2).

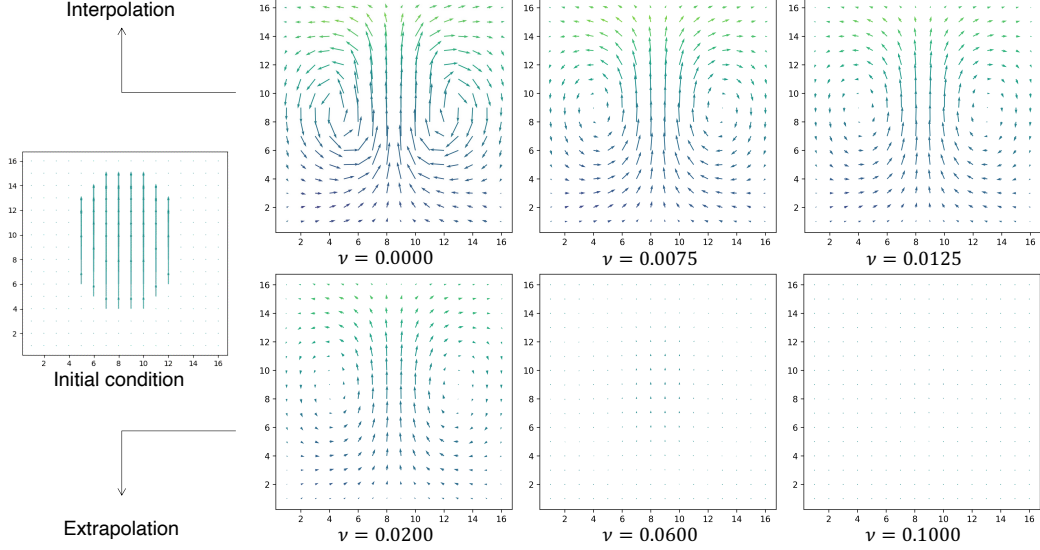


Figure 11: Fluid dynamics: our method captures the velocity fields of a wide range of viscous fluids. Large viscosity severely dissipates the velocity. All frames shown are captured from time step 25. The first row consists of the interpolated data while the second row consists of the extrapolated data.

For network hyperparameters, we adopt a latent space dimension $r = 6$ and a MLP width $\beta = 10$.

8.4 Training and Testing Data

We generate training data by varying the spatially-constant viscosity: $\mu = \nu \in \mathcal{D} = [0, 0.02] \subset \mathbb{R}$. We sample 3 different viscosities from \mathcal{D} . For each viscosity ν , we run a simulation of 50 time steps. In total, 150 time steps are used for training. For testing, we first sample 3 viscosity values from $\mathcal{D} = [0, 0.02]$. Furthermore, we also sample 3 values from the extrapolated region $\mathcal{D}^{\text{extrapolate}} = [0.02, 0.1]$. Notice how the extrapolated region has a larger range (0.08) than the interpolated region (0.02).

8.5 Results

Figure 11 demonstrates our method’s ability to qualitatively capture fluid dynamics with different viscosities on both interpolated data as well as extrapolated data. Surrogate models that predict velocity fields directly from viscosities (e.g., using a neural network) typically cannot handle extrapolation. By contrast, our approach handles extrapolated scenarios because we only approximate the spatial representation with a neural network, not the PDE itself. Therefore, as long as the extrapolated cases involve vector fields that can be represented by the low-dimensional implicit neural representation, our reduced-order solver is able to evolve the latent space vector to capture them according to the PDE.

9 Solid Mechanics

9.1 Continuous PDE

We solve the elastodynamics equation arisen from solid mechanics for deformable soft body modeling:

$$\rho_0 \ddot{\phi} = \nabla \cdot \mathbf{P}(\nabla \phi) + \rho_0 \mathbf{B},$$

where $\phi(\mathbf{X}, t)$ maps the undeformed (reference) position (\mathbf{X}) of an arbitrary material point from the reference configuration Ω to its deformed (current) position (\mathbf{x}) at time t . Proper Dirichlet and Neumann boundary conditions are applied.

We assume the first Piola–Kirchhoff stress \mathbf{P} is strictly a function of the deformation gradient $\mathbf{F} = \nabla \phi$. In particular, we adopt the corotated linear elasticity constitutive law,

$$\mathbf{P}(\mathbf{F}) = 2\mu(\mathbf{F} - \mathbf{R}) + \lambda \text{tr}^2(\mathbf{R}^T \mathbf{F} - \mathbf{I})\mathbf{R},$$

where \mathbf{R} is the rotation tensor from the polar decomposition of the deformation gradient $\mathbf{F} = \mathbf{R}\mathbf{S}$, λ and μ are the first lame parameter (Pa) and the second lame parameter / shear modulus (Pa). The proposed framework also works with other elasticity constitutive laws and can be easily extended to capture hysteresis and inelasticity.

9.2 Full-order Model

We adopt the tetrahedral-mesh-based linear finite element method (FEM) for the full-order model. We closely follow the course by Sifakis and Barbic (2012). Here we review only the salient features and refer to their work for theoretical and practical details.

We spatially discretize the domain of interest using linear tetrahedra. For each tetrahedron, we have four undeformed vertex positions $(\mathbf{X}_1, \dots, \mathbf{X}_4)$ and four deformed vertex positions $(\mathbf{x}_1, \dots, \mathbf{x}_4)$. For each vertex, we have $\mathbf{x}_i = \mathbf{F}\mathbf{X}_i + \mathbf{b}$, where \mathbf{b} is the translation.

Consequently, we can obtain the deformation gradient \mathbf{F} of each tetrahedron by solving $\mathbf{D}_s = \mathbf{F}\mathbf{D}_m$, where $\mathbf{D}_s = [\mathbf{x}_1 - \mathbf{x}_4 \quad \mathbf{x}_2 - \mathbf{x}_4 \quad \mathbf{x}_3 - \mathbf{x}_4]$ and $\mathbf{D}_m = [\mathbf{X}_1 - \mathbf{X}_4 \quad \mathbf{X}_2 - \mathbf{X}_4 \quad \mathbf{X}_3 - \mathbf{X}_4]$.

Furthermore, the internal elastic forces on the vertices $(\mathbf{f}_1, \dots, \mathbf{f}_4)$ can be computed though $[\mathbf{f}_1 \quad \mathbf{f}_2 \quad \mathbf{f}_3] = -\frac{1}{6}|\det \mathbf{D}_m| \mathbf{P}(\mathbf{F})\mathbf{D}_m^{-T}$ and $\mathbf{f}_4 = -\mathbf{f}_1 - \mathbf{f}_2 - \mathbf{f}_3$.

9.3 Reduced-order Model

Since the initial condition is known for a given problem, we opt to construct a low-dimensional manifold for the displacement field $\mathbf{u}(\mathbf{X}, t) = \phi - \mathbf{X}$. The deformation map can then be computed via $\phi = \mathbf{u} + \mathbf{X}$. The hyperparameters of the low-dimensional manifold are $r = 2$ and $\beta = 20$.

Unlike previously discussed PDEs, the elastodynamics equation is second-order in time. Consequently, in addition to the function value of the manifold, we also need to infer the temporal derivative during latent space dynamics. We do so by employing the tangent space of the manifold,

$$\dot{\phi}(\mathbf{x}, t_n) = \frac{\partial \mathbf{g}_{\theta_g}}{\partial \mathbf{q}} \dot{\mathbf{q}}_n.$$

To compute the acceleration (and increment the velocity) of a vertex belonging to the integration samples set \mathcal{M} , we need to evaluate the internal force at this particular vertex. We can calculate the vertex force by accumulating the internal forces of tetrahedra incident on this particular vertex. Tetrahedron forces are computed using the formula described in the previous section. To attain optimal gradient accuracy (Section 4.2), we opt to use finite element's linear basis function to compute the deformation gradient \mathbf{F} of each tetrahedron.

To compute these internal forces and deformation gradients, we also need to obtain the position information (via the low-dimensional manifold) of all vertices in the one-ring neighborhoods of the integration samples. We refer to the set of these neighboring vertices as \mathcal{N} . Therefore, the total number of spatial samples in the reduced-order model now becomes $|\mathcal{M}| + |\mathcal{N}|$. Since one-ring neighbors only entail a small subset of the original degrees of freedom, we still offer significant spatial sample reduction from the full order model (P).

9.4 Training and Testing Data

9.4.1 Gravity-induced Impact

An initially-static rectangular-shaped deformable object ($P = 2,065$ vertices and $9,346$ tetrahedra) accelerates due to downward gravity. After impacting the collision objects underneath, the material undergoes intense deformation.

We generate training and testing data by sampling the shear modulus $\mu = \mu \in \mathcal{D} = [60,000, 70,000] \subset \mathbb{R}$. The first lame parameter λ is fixed to be zero, in which case the corotated linear elasticity constitutive law simplifies to the As-Rigid-As-Possible energy (Sorkine and Alexa, 2007). Specifically, we uniformly generate 4 samples of the shear modulus for training data. We simulate 200 time steps for each shear modulus. Therefore, a total of 800 time steps are used for training. We then randomly generate 3 samples of the shear modulus from \mathcal{D} . We also simulate 200 time steps for these shear moduli and use them for testing.

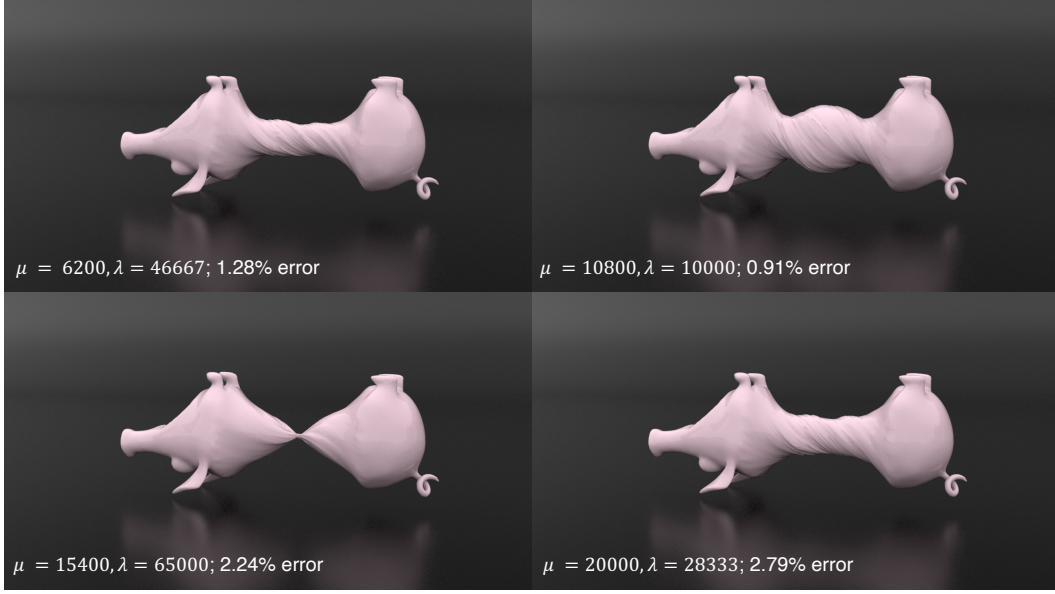


Figure 12: Our approach captures a wide range of elastic moduli with modest errors compared to the full-order ground truth.

9.4.2 Torsion and Tension

We study another common solid mechanics application where the material undergoes torsion and tension. The left and the right boundaries kinematically move at constant translational and angular velocities of the same magnitude but in opposite directions.

We solve the parameterized family of problem where $\mu = (\mu, \lambda) \in \mathcal{D} = [6, 200, 20, 000] \times [10, 000, 65, 000] \subset \mathbb{R}^2$. We obtain 9 training samples via uniform full-factorial sampling of the parameter space. We simulate 100 time steps for each training sample. We then use the Latin hypercube method to randomly generate another 4 testing samples. We also simulate 100 time steps for these testing samples.

9.5 Results

Figure 8 in the main text demonstrates a testing case ($\mu = 62500$, 2.68% error from the full-order ground truth) for the experiment from Section 9.4.1. Since our method is discretization-independent, we can optimally adapt the simulation resolution.

After training on the experiment from Section 9.4.2, our method captures a wide range of shearing and volume-preserving behaviors (see Figure 12).

10 Comparison with Prior Approaches

We compare our approach with prior reduced-order approaches that generate fast PDE solutions via latent space dynamics. Specifically, we compare our method with the widely adopted proper orthogonal decomposition (POD) method (Berkooz et al., 1993). SIREN, PINN, or GNN are related to our work but are very different in nature. While their goal is to directly solve PDEs with neural network architectures, our goal is to leverage neural networks for dimension reduction. Therefore, we do not compare with them and focus on comparison with other dimension reduction methods.

POD approximates the discretized vector field with a linear basis U ,

$$\vec{f}(t) = (f(x^1, t), \dots, f(x^i, t), \dots, f(x^P, t))^T = Uq(t),$$

where U is a matrix of size Pd by r . U is most easily constructed via a singular value decomposition of the discretized training data (Sifakis and Barbic, 2012).

We implement the POD approach in the same PyTorch framework as our approach. The two approaches share exactly the same PDE time-stepping algorithm (step 2) during latent space dynamics.

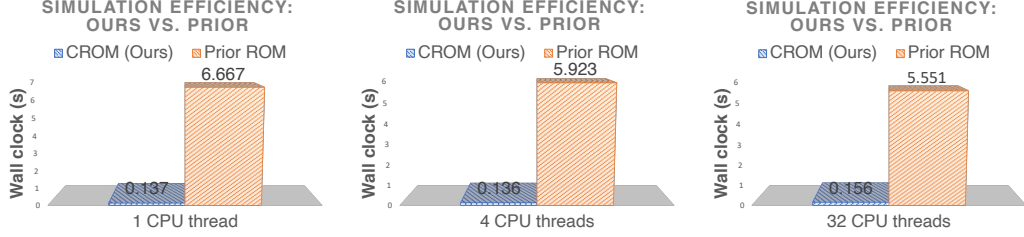


Figure 13: Wall clock time comparison with prior ROM approach. Our approach obtains considerable speedups across different computational resources.

For POD, the network inference step (step 1) and the network inversion step (step 3) employ the linear basis U instead of neural network weights.

10.1 Speed

We measure the wall-clock computation time during the falling stage (before contact) of the gravity-induced impact experiment (see Section 9.4.1 and Figure 8 in the main text). In particular, since all model reduction methods (including our approach and POD) share the same PDE time-stepping algorithm (step 2), we measure its wall-clock computation cost to ensure the generalizability of the comparison.

Since POD is baked into a particular discretization, it does not allow for adaptive discretization. Therefore, the high-resolution mesh (2,065 vertices, 9,346 tetrahedra) has to be used throughout the falling stage even though there is minimal deformation. Consequently, its computation cost is significantly higher than our approach, which employs a low-resolution mesh (8 vertices, 5 tetrahedra) during the falling stage. Figure 13 shows that our approach is faster than the POD approach with different CPU thread counts. Our method’s advantage is most obvious when there is extremely limited computational resource (1 CPU thread).

Hyper-reduction techniques (An et al., 2008), such as the integration samples introduced in our approach, can also be employed to speed up the high-resolution mesh solution by reducing spatial samples. However, this is orthogonal to our adaptive discretization contribution, and the hyper-reduction techniques can be employed to further accelerate the low-resolution mesh solution as well.

10.2 Memory

We compare the memory consumption of our method and POD with the same latent space dimension (r), both trained on data from the torsion and tension experiment (see Section 9.4.2). For all implicit neural representation networks, we set the MLP width to be $\beta = 20$. Independent of latent space dimension (r), our network has a near-constant memory consumption (see Figure 14). By contrast, the memory consumption of POD scales linearly with r . More importantly, since U is a Pd by r matrix, the memory consumption of POD scales linearly with the number of discretized positions P . Unlike POD, our approach’s memory consumption is independent of the number of spatial samples. Consequently, in this large-scale example that features $P = 66,608$ vertices, we observe more than ten-fold advantages with our method across all latent space dimensions (see Figure 14). It’s possible to reduce the memory cost of prior discretization-dependent ROM methods via discretization-specific architectures, such as convolution layers for grid data (Lee and Carlberg, 2020). However, the memory consumption still scales linearly with respect to the number of spatial samples.

Even though the overall memory consumption of our approach is significantly lower, our approach’s per-sample evaluation cost is higher. For any given discretized spatial sample, POD only requires a vector-matrix multiplication of a d by r matrix. By contrast, our approach needs to go through the entire MLP that employs $d\beta$ by $d\beta$ matrices.

10.3 Accuracy

Figure 4 demonstrates the accuracy of the networks studied in the previous memory section. Our method consistently offers orders-of-magnitude smaller training accuracies. This accuracy advantage

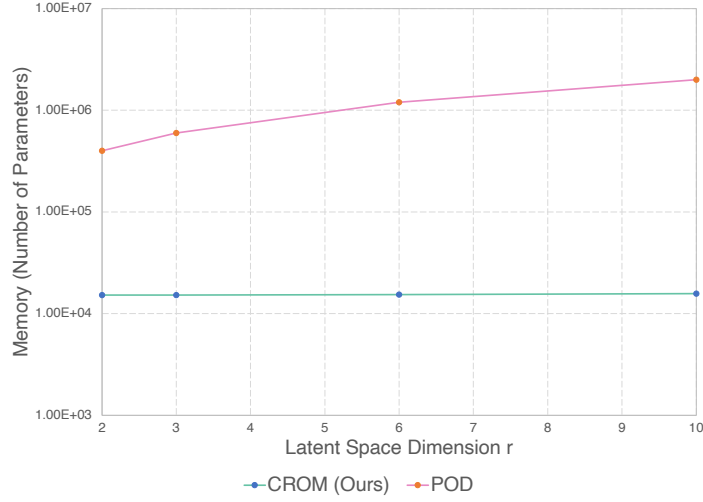


Figure 14: Memory consumption of the low-dimensional manifold. Our approach consistently consumes orders-of-magnitude less memory than the POD approach across all latent space dimensions.

is especially noticeable with small latent space dimensions (e.g., $r = 2$). Further increasing the latent space dimension leads to higher accuracies with POD but not our approach. As discussed in Section 5, our approach’s accuracy depends more saliently on the MLP width as opposed to the latent space dimension. Furthermore, unlike POD, the continuous low-dimensional manifold also facilitates accurate handling of adaptive spatiotemporal data (Pan et al., 2022).

In summary, our approach offers orders-of-magnitude advantages over prior model reduction approaches (specifically, POD) in terms of computation speed, memory, and accuracy.

11 Comparison with the Full-order Model

To gauge the practical performance of our approach over the full-order model, we measure the sheer wall-clock performances of our reduced-order model and the full-order model.

To facilitate fair comparison, we implement, optimize, and (fully) parallelize the full-order PDE solution and the reduced-order approach within the PyTorch framework (Paszke et al., 2019) without any other dependency. The full-order and reduced-order models share the same code for the PDE times-stepping module (step 2). To encourage fair comparison, for operations involving neural networks (step 1 and step 3), we do not use customized SIMD vectorizations, CUDA kernels, or highly optimized inference libraries such as TensorRT (Vanholder, 2016), though these optimizations should lead to a further performance gain of our algorithm. In addition, having both models implemented in the same framework allows us to compare them under the same computing environments, avoiding biased comparison where the full-order model runs on a significantly limited computing resource (e.g., 8-core CPU) while the reduced-order model runs on a high-performance computing device (e.g., 5120-core GPU).

Figure 15 reports the wall clock time of our reduced-order method and the full-order method across different computing platforms. While our approach is significantly faster on all computing platforms, its strongest speedup is obtained on the CPUs. This is unsurprising since the computationally expensive full-order model benefits more from high-end data-center GPUs (e.g., V100) than the reduced-order model. In addition, because the neural network in the reduced-order model only employs a few 60 by 60 matrices ($d = 3, \beta = 20$), inference on CPU is also efficient. This opens doors for employing our models on limited computing platforms such as mobile and VR devices.

Figure 16 further breaks down the computation time spent on each component of the reduced-order model. While the overhead of the neural network operations (step 1 and step 3) is non-negligible,

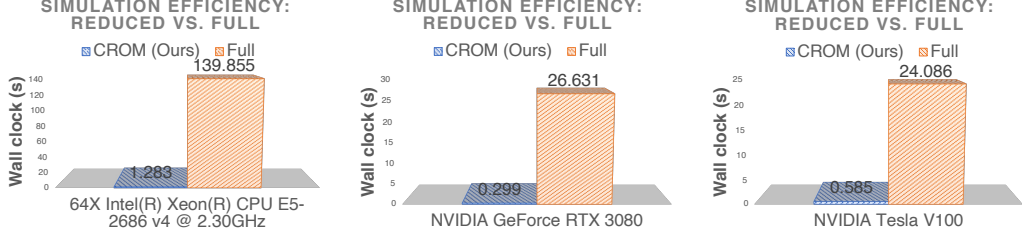


Figure 15: Wall clock time comparison with the full-order method. Our approach obtains significant speedups across different computing platforms.

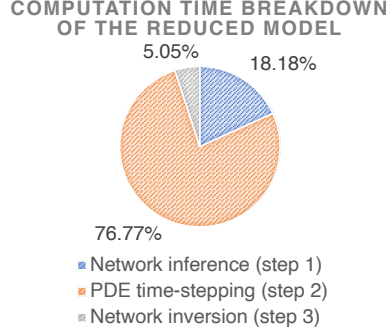


Figure 16: CROM timing breakdown. Neural network operations introduce minimal overhead. The computation bottleneck remains to be PDE time-stepping.

the bottleneck of the algorithm remains to be PDE time-stepping (step 2). In particular, the network inversion cost is very low, thanks to the linearized inversion solver discussed in Section 2.

Figure 17 reports the accuracy and the speed of our approach using different MLP layer widths (β), neural network inversion methods (nonlinear least squares (NLS) vs. linear least squares (LLS)), computing platforms (CPU vs. GPU), and integration sample sizes ($|\mathcal{M}|$). In general, we observe similar accuracies between NLS and LLS (e.g., $[\beta = 20, \text{LLS, GPUs, } |\mathcal{M}| = 40]$ vs. $[\beta = 20, \text{NLS, GPUs, } |\mathcal{M}| = 40]$), while LLS is significantly faster. Increasing sample size lead to higher accuracies but also require longer computation time (e.g., $[\beta = 5, \text{NLS, CPUs, } |\mathcal{M}| = 10]$ vs. $[\beta = 5, \text{NLS, CPUs, } |\mathcal{M}| = 40]$). Increasing the MLP layer width yields higher accuracies but also increases the computation time. In particular, the computation time is increased more on CPUs (e.g., $[\beta = 5, \text{LLS, CPUs, } |\mathcal{M}| = 40]$ vs. $[\beta = 20, \text{LLS, CPUs, } |\mathcal{M}| = 40]$) than on GPUs.

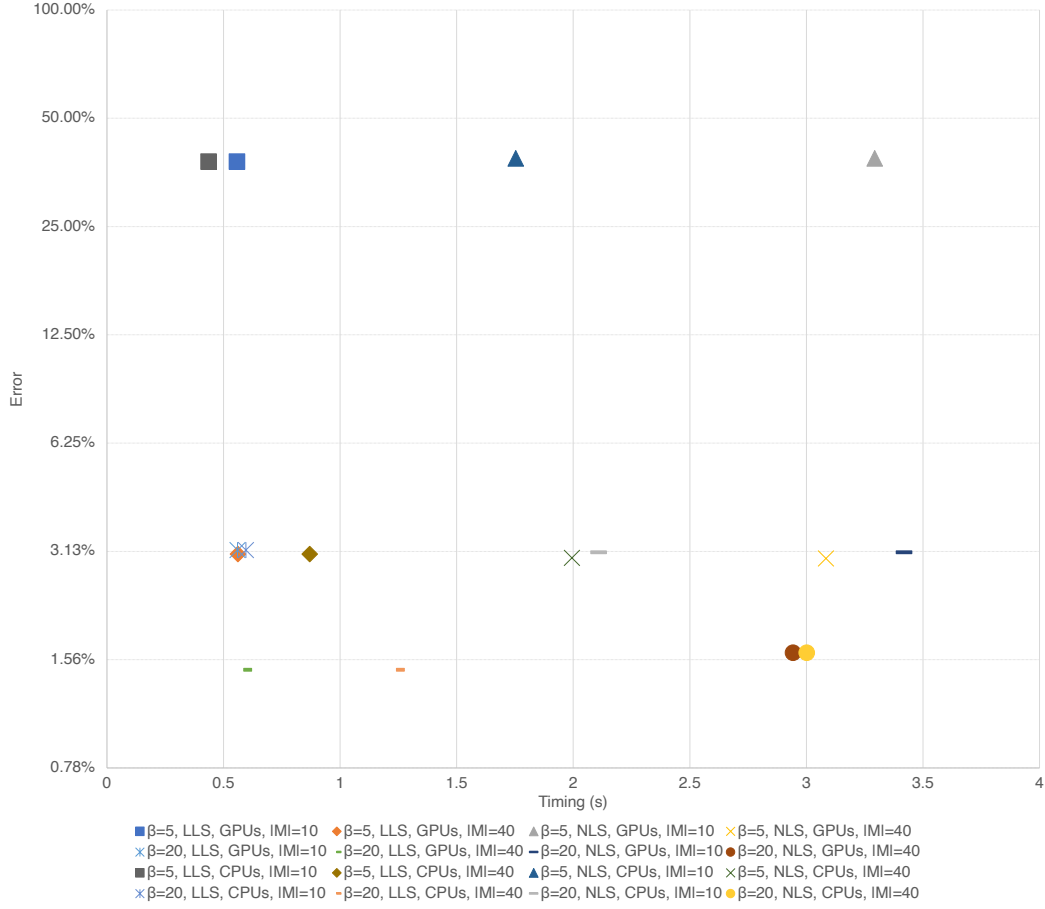


Figure 17: Accuracy vs. Speed: our approach under different setups. In comparison, the ground truth full-order takes 139.855s on CPUs and 24.086s on GPUs (see Figure 15). Our approach obtains significant speedups with less than 5% error under various settings.

References

- An, S.S., Kim, T., James, D.L., 2008. Optimizing cubature for efficient integration of subspace deformations. *ACM transactions on graphics (TOG)* 27, 1–10.
- Berkooz, G., Holmes, P., Lumley, J.L., 1993. The proper orthogonal decomposition in the analysis of turbulent flows. *Annual review of fluid mechanics* 25, 539–575.
- Cannon, J.R., 1984. *The one-dimensional heat equation*. 23, Cambridge University Press.
- Chen, P.Y., Chiaramonte, M., Grinspun, E., Carlberg, K., 2021. Model reduction for the material point method via an implicit neural representation of the deformation map. *arXiv preprint arXiv:2109.12390*.
- Chorin, A.J., 1968. Numerical solution of the navier-stokes equations. *Mathematics of computation* 22, 745–762.
- Clevert, D.A., Unterthiner, T., Hochreiter, S., 2015. Fast and accurate deep network learning by exponential linear units (elus). *arXiv preprint arXiv:1511.07289*.
- Du, Y., Collins, K., Tenenbaum, J., Sitzmann, V., 2021. Learning signal-agnostic manifolds of neural fields. *Advances in Neural Information Processing Systems* 34, 8320–8331.
- Falcon et al., W., 2019. Pytorch lightning. *GitHub*. Note: <https://github.com/PyTorchLightning/pytorch-lightning> 3.
- Hertz, A., Perel, O., Giryes, R., Sorkine-Hornung, O., Cohen-Or, D., 2021. Sape: Spatially-adaptive progressive encoding for neural optimization. *Advances in Neural Information Processing Systems* 34.
- Kingma, D.P., Ba, J., 2014. Adam: A method for stochastic optimization. *arXiv preprint arXiv:1412.6980*.
- Lee, K., Carlberg, K.T., 2020. Model reduction of dynamical systems on nonlinear manifolds using deep convolutional autoencoders. *Journal of Computational Physics* 404, 108973.
- Liu, H.T.D., Williams, F., Jacobson, A., Fidler, S., Litany, O., 2022. Learning smooth neural functions via lipschitz regularization. *arXiv preprint arXiv:2202.08345*.
- Nocedal, J., Wright, S., 2006. *Numerical optimization*. Springer Science & Business Media.
- Pan, S., Brunton, S.L., Kutz, J.N., 2022. Neural implicit flow: a mesh-agnostic dimensionality reduction paradigm of spatio-temporal data. *arXiv preprint arXiv:2204.03216*.
- Paszke, A., Gross, S., Massa, F., Lerer, A., Bradbury, J., Chanan, G., Killeen, T., Lin, Z., Gimelshein, N., Antiga, L., et al., 2019. Pytorch: An imperative style, high-performance deep learning library. *Advances in neural information processing systems* 32.
- Perona, P., Malik, J., 1990. Scale-space and edge detection using anisotropic diffusion. *IEEE Transactions on pattern analysis and machine intelligence* 12, 629–639.
- Sifakis, E., Barbic, J., 2012. Fem simulation of 3d deformable solids: a practitioner’s guide to theory, discretization and model reduction, in: *Acm siggraph 2012 courses*, pp. 1–50.
- Sitzmann, V., Martel, J., Bergman, A., Lindell, D., Wetzstein, G., 2020. Implicit neural representations with periodic activation functions. *Advances in Neural Information Processing Systems* 33.
- Sorkine, O., Alexa, M., 2007. As-rigid-as-possible surface modeling, in: *Symposium on Geometry processing*, pp. 109–116.
- Stam, J., 1999. Stable fluids, in: *Proceedings of the 26th annual conference on Computer graphics and interactive techniques*, pp. 121–128.
- Vanholder, H., 2016. Efficient inference with tensorrt, in: *GPU Technology Conference*, p. 2.
- Yang, G., Belongie, S., Hariharan, B., Koltun, V., 2021. Geometry processing with neural fields. *Advances in Neural Information Processing Systems* 34.